Available online at www.sciencedirect.com
ScienceDirect
Journal of Computational Physics 217 (2006) 424–452
JOURNAL OF COMPUTATIONAL PHYSICS
www.elsevier.com/locate/jcp

A fictitious domain method for particulate flows with heat transfer

Zhaosheng Yu [a,*], Xueming Shao [b], Anthony Wachs [c]

[a] Faculty of Science and Technology, Department of Applied Physics, Physics of Complex Fluids, University of Twente, P.O. Box 217, 7500AE Enschede, The Netherlands
[b] Institutue of Fluid Engineering, Zhejiang University, 310027 Hangzhou, China
[c] Fluid Mechanics Department, Institut Français du Pétrole, 1 & 4, avenue de Bois Préau, 92852 Rueil Malmaison Cedex, France

Received 27 September 2005; received in revised form 6 January 2006; accepted 6 January 2006
Available online 17 February 2006

Abstract

The distributed-Lagrange-multiplier/fictitious-domain (DLM/FD) method of Glowinski et al. [R. Glowinski, T.-W. Pan, T.I. Hesla, D.D. Joseph, A distributed Lagrange multiplier/fictitious domain method for particulate flows, Int. J. Multiphase Flow 25 (1999) 755–794] is extended to deal with heat transfer in particulate flows in two dimensions. The Boussinesq approximation is employed for the coupling between the flow and temperature fields. The fluid-flow equations are solved with the finite-difference projection method on a half-staggered grid. In our operator splitting scheme, the Lagrange multipliers at the previous time level are kept in the fluid equations, and the new Lagrange multipliers for the rigid-body motion constraint and the Dirichlet temperature boundary condition are determined from the reduced saddle-point problem, whereas a very simple scheme based on the fully explicit computation of the Lagrange multiplier is proposed for the problem in which the solid heat conduction inside the particle boundary is also considered. Our code for the case of fixed temperature on the immersed boundary is verified by comparing favorably our results on the natural convection driven by a hot cylinder eccentrically placed in a square box and on the sedimentation of a cold circular particle in a vertical channel to the data in the literature. The code for the case of freely varying temperature on the boundaries of freely moving particles is applied to analyze the motion of a catalyst particle in a box and in particular the heat conductivities of nanofluids and sheared non-colloidal suspensions, respectively. Our preliminary computational results support the argument that the micro-heat-convection in the fluids is primarily responsible for the unusually high heat conductivity of nanofluids. It is shown that the Peclet number plays a negative role in the diffusion-related heat conductivity of a sheared non-colloidal suspension, whereas the Reynolds number does the opposite.

Keywords: Fictitious domain method; Distributed Lagrange multiplier; Particulate flows; Heat transfer; Heat conductivity; Nanofluids

* Corresponding author. Tel.: +31 53 4893093; fax: +31 53 4891096.
E-mail address: z.yu@tnw.utwente.nl (Z. Yu).

0021-9991/$ - see front matter
doi:10.1016/j.jcp.2006.01.016

1. Introduction

Particulate flows are widespread in nature and industrial applications. With the rapid development of computer power, the direct numerical simulation (DNS), based on the Navier–Stokes equations or the discrete lattice-Boltzmann equation for the solution of the fluid-flow problem, has become a practical and important tool to probe the mechanics in particulate flows. Over the past decade a variety of DNS methods have been proposed. They can be classified into two families: boundary-fitted methods and non-boundary-fitted methods, according to whether or not the boundary-fitted mesh is used for the solution of the flow field. For the boundary-fitted methods such as the arbitrary Lagrangian–Eulerian (ALE) finite-element method (FEM) [1], the fluid flow is computed on a boundary-fitted mesh and remeshing is normally required as the interfaces move, whereas for the non-boundary-fitted methods such as the lattice Boltzmann method (LBM) [2], the immersed boundary (IB) method [3], the distributed Lagrange multiplier based fictitious domain method (DLM/FD) [4], the accelerated Stokesian dynamics (ASD) [5] and the force coupling method (FCM) [6,7], the fluid flow is computed on a stationary grid constructed in the entire domain comprising both the exterior and interior of the particles. The non-boundary-fitted methods are, generally speaking, simpler and more efficient than the boundary-fitted methods, in particular for the simulation of concentrated suspensions.

The fictitious domain (FD) method was initially developed to solve partial differential equations in a complex geometry, as pointed by Glowinski et al. [4]. Glowinski et al. [8–11] described the FD methods for the Dirichlet problem in which the boundary condition is enforced with the Lagrange multiplier method, and they employed the methods to solve some differential equations and the incompressible viscous unsteady flows in complex or moving geometries. The Lagrange multiplier based FD method was also used by Bertrand et al. [12] and Tanguy et al. [13] to calculate the three-dimensional Stokes flows of Newtonian and viscoplastic fluids in a mixer. Glowinski et al. [4] developed the distributed Lagrange multiplier based FD method (DLM/FD) to simulate particulate flows where the rigid particles move freely. The key idea in this method is that the interior domains of the particles are filled with the same fluids as the surroundings and the Lagrange multiplier (physically a pseudo body force) is introduced to enforce the interior (fictitious) fluids to satisfy the constraint of rigid body motion. The method has been successfully applied to the simulation of particulate flows [14–16]. Compared to the lattice Boltzmann method, the DLM/FD method has an advantage of flexibility in the sense that it can be easily extended to any phenomenological equations, whereas the extension of the lattice Boltzmann method to a complex fluid needs invoking the statistical physics, and indeed the application of the DLM/FD method to the simulation of particulate suspensions of viscoelastic fluids appears more successful [15,17]. The present work is also an example demonstrating the flexibility of the DLM/FD method. The DLM/FD method and the immersed boundary (IB) method proposed by Höfler and Schwarzer [3] that is built on the original IB method of Peskin for fluid/flexible-body interactions [18] have much in common: both introduce a pseudo body force that is associated with the rigid-body motion of the fictitious fluids inside the particle boundaries, and the hydrodynamic forces on the particles can be computed with the pseudo body force. In fact, the two methods can be viewed as the different numerical implementations of a general DLM/FD formulation [19] for fluid/solid systems. The main difference is that for the former the Lagrange multiplier (i.e., the pseudo body force) is normally determined implicitly from the kinematic constraint of the solid velocity being equal to the fluid velocity (the rigid-body motion constraint in case of rigid particles), whereas for the latter the solid velocity is explicitly set to the same as the most recently calculated fluid velocity and the pseudo body force is subsequently evaluated based on the motion of the solid (a sufficiently large elastic spring constant or elastic modulus in case of rigid particles). Due to implicit calculation of the pseudo body force, the DLM/FD method is computationally more expensive but presumably more robust than the IB method. Nevertheless, the line between the DLM/FD and IB methods is not distinct due to the fact that one may easily replace the implicit scheme with the explicit scheme for the Lagrange multiplier in the DLM/FD method, such as the one proposed by Shi and Phan-Thien [20] for fluid–structure interactions and the simple scheme to be presented later in the present study for the solution of the combined fluid/solid temperature equation. One drawback of the DLM/FD method for the particulate flows is that the formulation requires a discontinuous velocity gradient across the particle boundary, which cannot be well treated with the non-boundary-fitted mesh. This drawback, however, is alleviated by the fact that the hydrodynamic force on the particles is of most

interest for the particulate suspensions and can be obtained with reasonable accuracy since the hydrodynamic force is determined from integration of the pseudo body force over the solid body and is not sensitive to the quality of the local solution around the boundary, which is not surprising since the local solution in the solid domain obtained from the DLM/FD method, though not very smooth, well satisfies the rigidity constraint in a weak form and consequently well conserves the momentum of the combined fluid/solid system.

For the Dirichlet problem, the body-force-base FD and IB methods are characterized by a direct introduction of the pseudo body force adjusting the velocities on the nodes in the vicinity of the boundary and rendering them to satisfy the boundary condition via interpolation to the boundary. In contrast, some IB methods [21] do not invoke the pseudo body force directly, and the no-slip condition on the solid boundary is fulfilled via the interpolation (or extrapolation) of the velocity on the boundary to the fluid nodes nearby (one may still get a momentum forcing for these nodes as a result of the interpolation, but such methods are clearly different from the direct pseudo-body-force-based methods); the equations for the fictitious fluid nodes inside the solid boundary may be retained [22] or discarded (known as ghost-cell IB methods [21]). These non-body-force-based (or direct-interpolation-based) IB methods have been proved very successful for the cases where the motion of the boundary is prescribed in advance [21], but it remains to see whether they can perform better than the aforementioned body-force-based FD or IB methods for the particulate flows. There exist a variety of different implementations of the body-force-based non-boundary-fitted methods for the particulate flows in the literature (e.g. [4,3,16,17,24–28]). It should be noted that in above discussions we do not distinguish between the pseudo body force and the general momentum forcing since any forcing term in the momentum equation can be made equivalent to a pseudo body force; the Lagrange multiplier is introduced exactly in a form of body force when the L^2 inner product is used for the Lagrange multiplier term in the weak DLM/FD formulation [4], but can be in other forms according to other definitions of the inner product [4], and even in a form of stress in the formulation of Patankar et al. [23].

Recently, the DLM/FD method has been extended by Baaijens [29] and Yu [19] to handle the fluid/elastic–structure interactions. The aim of the present study is to extend the DLM/FD method to particulate flows where the heat transfer between the particles and fluids needs to be accounted for. The work was motivated by the fact that in many industrial applications the motion of the particles and the heat transfer are strongly coupled. For example, in the fluidized-bed reactor, highly active catalysts are used because they can make the processes for the polymerization of olefins using ''low pressure processes'' very attractive, however, there is a danger that the catalysts might melt if the heat produced from the chemical reaction cannot be rapidly removed from the catalysts [30]. The interactions between catalyst particles were observed to affect the heat removal significantly [30], therefore, full resolution of the motion of catalysts and the heat transfer is definitely desirable. Another example is ''nanofluids'', a colloidal suspension of nanoparticles or nanofibers with sizes typically of 1–100 nm. Nanofluids have attracted great interest recently because of reports of greatly enhanced thermal properties. For example, a small amount ($<$1% volume fraction) of Cu nanoparticles dispersed in ethylene glycol was reported to increase the heat conductivity of the liquid by 40% [31]. The traditional effective medium theory for the composite materials such as the Maxwell–Garnett (MG) model [32] fails to explain such a significant enhancement in the heat conductivity, and a variety of ideas have been proposed to elucidate this anomalous phenomenon [31]. Recently, Prasher et al. [33] has excluded some possible mechanisms through an order-of-magnitude analysis and showed that convection caused by the Brownian movement of the nanoparticles is primarily responsible for the enhancement in the heat conductivity of nanofluids [34]. However, the authors established the model for predicting the thermal conductivity by the empirical combination of the parameters based on data from Nusselt correlation for particle-to-fluid heat transfer in fluidized beds, and the exact origin of the empirical constants is not understood. Clearly, only a direct simulation of the Brownian motion of nanoparticles together with the thermal convection can provide deep insight into the mechanism by which the thermal conductivity is enhanced and thereby a solid foundation for the application of the nanofluids associated with its unusual thermal properties.

For the simulation of heat transfer in the solid/fluid system the boundary-fitted methods have been predominantly used. For example, with commercial software, McKenna et al. [30] studied the heat transfer from catalyst spheres, and Nijemeisland and Dixon [35] investigated the heat transfer in a fixed bed of spheres. Gan et al. [36,37] numerically simulated the sedimentation of solid particles with thermal convection using the ALE finite-element method, and these two are the only numerical works we found in the literature for the case

where both the motion of the particles and the heat transfer are considered, however, the authors imposed a fixed temperature on the particle boundary, which is an unrealistic boundary condition. There are very limited works involving the application of the non-boundary-fitted methods to the heat transfer problems. Kim and Choi [38] and Pacheco et al. [39] developed the immersed-boundary finite-volume method for the heat transfer in complex geometries, respectively, where no particle motion is considered. In the present study, we not only show that the DLM/FD method is a reliable and efficient method for the heat transfer problem in complex geometries, but also extend the method to a new field: particulate flows where heat conduction inside the moving particles and thermal convection in the fluids are coupled.

The rest of the paper is organized as follows: we first derive a new combined temperature DLM/FD formulation for the case of freely varying temperature on the particle boundary, present the governing equations for the flow based on the Boussinesq approximation, and describe our computational scheme in the following section. We then verify our method for the case of fixed temperature on the boundary by comparing our results on the natural convection driven by a hot cylinder placed eccentrically in a square enclosure and the sedimentation of a cold particle in a vertical channel to the data available in the literature. For the case of freely varying temperature on the boundary, we show that our method is able to produce mesh-size and time-step convergent results in a test problem: motion of a catalyst particle in an enclosed box. The method is then applied to the preliminary analysis of the heat conductivity of sheared non-Brownian suspensions and nanofluids, respectively. Concluding remarks are given in the final section.

2. Numerical model

A schematic diagram of the fictitious domain method is depicted in Fig. 1. We only consider the 2D case in this study, however, the extension of the algorithm to the 3D case is straightforward. For simplicity of description, only one particle is considered. Let $P(t)$ and $\partial P(t)$ represent the solid domain and its boundary, Ω the entire domain comprising both interior and exterior of the body, and Γ the boundary of Ω. We assume a Dirichlet boundary condition on the outer boundary Γ for both velocities and temperature for convenience of exposition.

2.1. DLM/FD formulation for temperature equation

2.1.1. The case of freely varying temperature on the particle boundary

1. Fluid temperature equation:

$$\rho_f c_{pf} \frac{dT_f}{dt} = k_f \nabla^2 T_f + Q_f \quad \text{in } \Omega \setminus P(t), \tag{1}$$

$$T_f = T_\Gamma \quad \text{on } \Gamma. \tag{2}$$

2. Solid temperature equation:

$$\rho_s c_p \frac{dT_s}{dt} = k_s \nabla^2 T_s + Q_s \quad \text{in } P(t). \tag{3}$$

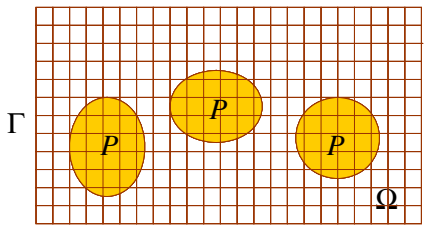

Fig. 1. Schematic diagram of the fictitious domain method.

The fluid and solid temperatures are coupled via:

$$T_f = T_s \quad \text{on } \partial P, \tag{4}$$

$$k_f \frac{\partial T_f}{\partial \mathbf{n}} = k_s \frac{\partial T_s}{\partial \mathbf{n}} \quad \text{on } \partial P. \tag{5}$$

In the above equations, T_f, ρ_f, c_{pf}, k_f, and Q_f denote the fluid temperature, density, heat capacity (or specific heat), heat conductivity, and heat source, respectively, and T_s, ρ_s, c_{ps}, k_s, and Q_s are corresponding solid quantities. In (4), $\mathbf{n}$ is the normal unit vector on the solid surface directing inwards the fluid. In (1), we neglect the contribution from the viscous dissipation, but it can be included in the heat source Q_f, if necessary. Note that in the above equations, '$\frac{d(\,)}{dt}$' represents the material derivative. If a quantity T is described in the Eulerian frame, then $\frac{dT}{dt} = \frac{\partial T}{\partial t} + \mathbf{u} \cdot \nabla T$, here $\mathbf{u}$ being the velocity.

Next, we follow the procedure of Glowinski et al. [4] and Yu [19] to derive the FD/DLM formulation for the heat transfer problem specified above.

Weak form: We define the following combined temperature space,

$$\Theta_T = \{(T_f, T_s) | T_f \in H^1(\Omega \setminus P), \quad T_s \in H^1(P), \qquad T_f = T_s \text{ on } \partial P,\ T_f = T_\Gamma \text{ on } \Gamma\}, \tag{6}$$

and corresponding combined variance space

$$\Theta_0 = \{(\Upsilon_f, \Upsilon_s) | \Upsilon_f \in H^1(\Omega \setminus P), \quad \Upsilon_s \in H^1(P), \qquad \Upsilon_f = \Upsilon_s \text{ on } \partial P,\ \Upsilon_f = 0 \text{ on } \Gamma\}, \tag{7}$$

and perform the following symbolic operations:

$$\int_{\Omega \setminus P} \text{Eq. (1) } \Upsilon_f \, d\mathbf{x} + \int_P \text{Eq. (3) } \Upsilon_s \, d\mathbf{x}. \tag{8}$$

Integrating the diffusion terms by parts and considering (5), we get

$$\int_{\Omega \setminus P} \left(\rho_f c_{pf} \frac{dT_f}{dt} - Q_f\right) \Upsilon_f \, d\mathbf{x} + \int_{\Omega \setminus P} k_f \nabla T_f \cdot \nabla \Upsilon_f \, d\mathbf{x} + \int_P \left(\rho_s c_{ps} \frac{dT_s}{dt} - Q_s\right) \Upsilon_s \, d\mathbf{x} + \int_P k_s \nabla T_s \cdot \nabla \Upsilon_s \, d\mathbf{x} = 0 \quad \text{for all } (\Upsilon_f, \Upsilon_s) \in \Theta_0. \tag{9}$$

The heat flux through the particle boundary vanishes in the combined temperature equation (9), since they represent an *internal* heat flux for the combined system, which is much like the case of the combined momentum equation where the hydrodynamic force on the particle boundary vanishes since it becomes an internal force for the combined system [4].

FD weak formulation: To construct a fictitious domain formulation, we extend the fluid computational domain from $\Omega \setminus P$ to Ω, and couple the temperatures T_f and T_s not only via the particle surface ∂P, but the entire solid domain P. The combined temperature and variance spaces are modified as follows:

$$\widetilde{\Theta}_T = \{(T_f, T_s) | T_f \in H^1(\Omega), \quad T_s \in H^1(P), \qquad T_f = T_s \text{ in } P,\ T_f = T_\Gamma \text{ on } \Gamma\}, \tag{10}$$

$$\widetilde{\Theta}_0 = \{(\Upsilon_f, \Upsilon_s) | \Upsilon_f \in H^1(\Omega), \quad \Upsilon_s \in H^1(P), \qquad \Upsilon_f = \Upsilon_s \text{ in } P,\ \Upsilon_f = 0 \text{ on } \Gamma\}. \tag{11}$$

Noting that

$$\int_P \left(\rho_f c_{pf} \frac{dT_f}{dt} - Q_f\right) (\Upsilon_f - \Upsilon_s) \, d\mathbf{x} + \int_P k_f \nabla T_f \cdot \nabla (\Upsilon_f - \Upsilon_s) \, d\mathbf{x} = 0 \quad \text{for all } (\Upsilon_f, \Upsilon_s) \in \widetilde{\Theta}_0 \tag{12}$$

and adding (12) to (9), we obtain the following FD-based weak formulation for $(T_f, T_s) \in \widetilde{\Theta}_T$

$$\int_\Omega \left(\rho_f c_{pf} \frac{dT_f}{dt} - Q_f\right) \Upsilon_f \, d\mathbf{x} + \int_\Omega k_f \nabla T_f \cdot \nabla \Upsilon_f \, d\mathbf{x} + \int_P \left[(\rho_s c_{ps} - \rho_f c_{pf}) \frac{dT_s}{dt} - (Q_s - Q_f)\right] \Upsilon_s \, d\mathbf{x} + \int_P (k_s - k_f) \nabla T_s \cdot \nabla \Upsilon_s \, d\mathbf{x} = 0 \quad \text{for all } (\Upsilon_f, \Upsilon_s) \in \widetilde{\Theta}_0. \tag{13}$$

DLM/FD weak formulation: Finally, the distributed Lagrange multiplier is introduced to relax the constraints '$T_f = T_s$ in P' from the combined temperature space and the corresponding constraint from the combined variance space, leading (13) to the following DLM/FD formulation for $T_f \in \overline{\Theta}_T$, $T_s \in H^1(P)$ and $\lambda_T \in \Lambda(P)$:

$$\int_\Omega \left(\rho_f c_{pf}\frac{dT_f}{dt} - Q_f\right)\Upsilon_f\,d\mathbf{x} + \int_\Omega k_f \nabla T_f \cdot \nabla \Upsilon_f\,d\mathbf{x} = \int_P \lambda_T \Upsilon_f\,d\mathbf{x} \quad \text{for all } \Upsilon_f \in \overline{\Theta}_0, \tag{14}$$

$$\int_P \left[(\rho_s c_{ps} - \rho_f c_{pf})\frac{dT_s}{dt} - (Q_s - Q_f)\right]\Upsilon_s\,d\mathbf{x} + \int_P (k_s - k_f)\nabla T_s \cdot \nabla \Upsilon_s\,d\mathbf{x} = -\int_P \lambda_T \Upsilon_s\,d\mathbf{x} \quad \text{for all } \Upsilon_s \in H^1(P), \tag{15}$$

$$\int_P (T_f - T_s)\zeta_T\,d\mathbf{x} = 0 \quad \text{for all } \zeta_T \in \Lambda(P), \tag{16}$$

where λ_T and ζ_T are the distributed Lagrange multiplier and its variance for the temperature defined in an appropriate space $\Lambda(P)$, respectively, and

$$\overline{\Theta}_T = \{T_f | T_f \in H^1(\Omega), \quad T_f = T_\Gamma \text{ on } \Gamma\}, \tag{17}$$

$$\overline{\Theta}_0 = \{\Upsilon_f | \Upsilon_f \in H^1(\Omega), \quad \Upsilon_f = 0 \text{ on } \Gamma\}. \tag{18}$$

In this study, we use the collocation-point-like method [19] to enforce the two temperatures to equal each other. The method is resulted from taking $\Lambda(P)$ as $H^1(P)$ and using the trapezoidal rule to perform the integration on discrete solid elements.

2.1.2. The case of fixed temperature on the particle boundary

If the temperature on the particle boundary is fixed, then the solution of the solid temperature is not necessary and we only need to enforce the Dirichlet boundary condition via a Lagrange multiplier defined on the particle boundary (Glowinski et al. [8]). The DLM/FD formulation in this case reads: find $T_f \in \overline{\Theta}_T$, and $\lambda_T \in L^2(\partial P)$, satisfying:

$$\int_\Omega \left(\rho_f c_{pf}\frac{dT_f}{dt} - Q_f\right)\Upsilon_f\,d\mathbf{x} + \int_\Omega k_f \nabla T_f \cdot \nabla \Upsilon_f\,d\mathbf{x} = \int_P \lambda_T \Upsilon_f\,d\mathbf{x} \quad \text{for all } \Upsilon_f \in \overline{\Theta}_0, \tag{19}$$

$$\int_{\partial P} (T_f - T_b)\zeta_T\,d\mathbf{x} = 0 \quad \text{for all } \zeta_T \in L^2(\partial P), \tag{20}$$

where T_b is the given temperature on the particle boundary.

2.2. DLM/FD formulation for flow

The combined momentum equations have been derived by Glowinski et al. [4] as follows:

$$\int_\Omega \left(\rho_f \frac{d\mathbf{u}}{dt} - \rho_f \mathbf{g}\right)\cdot \mathbf{v}\,d\mathbf{x} + \int_\Omega \boldsymbol{\sigma} : \nabla \mathbf{v}\,d\mathbf{x} - \int_P \boldsymbol{\lambda}\cdot\mathbf{v}\,d\mathbf{x} = 0, \tag{21}$$

$$\int_\Omega q\nabla\cdot\mathbf{u}\,d\mathbf{x} = 0, \tag{22}$$

$$\left(1 - \frac{\rho_f}{\rho_s}\right)\left[M\frac{d\mathbf{U}}{dt}\cdot\mathbf{V} + J\frac{d\boldsymbol{\omega}}{dt}\cdot\boldsymbol{\xi}\right] - \int_P (\rho_s - \rho_f)\mathbf{g}\cdot(\mathbf{V} + \boldsymbol{\xi}\times\mathbf{r})\,d\mathbf{x} + \int_P \boldsymbol{\lambda}\cdot(\mathbf{V} + \boldsymbol{\xi}\times\mathbf{r})\,d\mathbf{x} = 0, \tag{23}$$

$$\int_P [\mathbf{u} - (\mathbf{U} + \boldsymbol{\omega}\times\mathbf{r})]\cdot\boldsymbol{\zeta}\,d\mathbf{x} = 0, \tag{24}$$

where $\mathbf{u}$ and $\boldsymbol{\sigma}$ are the fluid velocity and stress, M, J, $\mathbf{U}$ and $\boldsymbol{\omega}$ the particle mass, moment of inertia, translational velocity and angular velocity, $\boldsymbol{\lambda}$ the distributed Lagrange multiplier for the rigidity constraint, $\mathbf{g}$ the gravitational acceleration, $\mathbf{r}$ the position vector with respect to the particle mass center, and $\mathbf{v}$, q, $\mathbf{V}$, $\boldsymbol{\xi}$, $\boldsymbol{\zeta}$ the variances for the fluid velocity, the fluid pressure, the particle translational and angular velocities, and the Lagrange multiplier, respectively.

We now consider the coupling between the temperature and flow fields. Generally speaking, the change in the temperature would affect all physical parameters of the fluids. However, to reasonably simplify the computation, the Boussinesq approximation is commonly used, which states that the variance in the temperature does not influence the fluid properties except for the density in the gravitational term. We may further assume the same for the effect of the temperature on the solid properties for the case where the solid temperature is considered. The relationship between the density in the gravitational term and the temperature reads:

$$\rho_f = \rho_{f0}[1 - \beta_f(T_f - T_0)], \tag{25}$$

$$\rho_s = \rho_{s0}[1 - \beta_s(T_s - T_0)], \tag{26}$$

where ρ_{f0} represents the reference density of the fluids at the reference temperature T_0, β_f the fluid heat expansion coefficient, and ρ_{s0} and β_s the solid reference density and heat expansion coefficient, respectively. Substituting (25) and (26) into (21)–(24) yields:

$$\int_\Omega \rho_{f0}\left(\frac{d\mathbf{u}}{dt} - \mathbf{g}\right)\cdot\mathbf{v}\,d\mathbf{x} + \int_\Omega \rho_{f0}\beta_f(T_f - T_0)\mathbf{g}\cdot\mathbf{v}\,d\mathbf{x} + \int_\Omega \boldsymbol{\sigma} : \nabla\mathbf{v}\,d\mathbf{x} - \int_P \boldsymbol{\lambda}\cdot\mathbf{v}\,d\mathbf{x} = 0, \tag{27}$$

$$\int_\Omega q\nabla\cdot\mathbf{u}\,d\mathbf{x} = 0, \tag{28}$$

$$\left(1 - \frac{\rho_{f0}}{\rho_{s0}}\right)\left[M\left(\frac{d\mathbf{U}}{dt} - \mathbf{g}\right)\cdot\mathbf{V} + J\frac{d\boldsymbol{\omega}}{dt}\cdot\boldsymbol{\xi}\right] + \int_P (\rho_{s0}\beta_s - \rho_{f0}\beta_f)(T_f - T_0)\mathbf{g}\cdot(\mathbf{V} + \boldsymbol{\xi}\times\mathbf{r})\,d\mathbf{x} + \int_P \boldsymbol{\lambda}\cdot(\mathbf{V} + \boldsymbol{\xi}\times\mathbf{r})\,d\mathbf{x} = 0, \tag{29}$$

$$\int_P [\mathbf{u} - (\mathbf{U} + \boldsymbol{\omega}\times\mathbf{r})]\cdot\boldsymbol{\zeta}\,d\mathbf{x} = 0. \tag{30}$$

In (29), T_f can be written as T_s if T_s in the solid domain is considered, since they are equal to each other in P.

2.3. Dimensionless governing equations

The governing equations discussed above can be non-dimensionalized by introducing the following scales: L_c for length, U_c for velocity, L_c/U_c for time, $\rho_{f0}U_c^2$ for the pressure p, and $\rho_{f0}U_c^2/L_c$ for the Lagrange multiplier. For convenience, we write the dimensionless quantities in the same form as their dimensional counterparts, unless otherwise specified. There normally exist two characteristic temperatures for the thermal problem, and we define one as T_0 and the other as T_m. Then the dimensionless temperature can be defined by $\overline{T} = \frac{T - T_0}{T_m - T_0}$. From (27)–(30), we get the dimensionless governing equations for the incompressible flows of Newtonian fluids as follows:

$$\int_\Omega \left(\frac{\partial\mathbf{u}}{\partial t} + \mathbf{u}\cdot\nabla\mathbf{u}\right)\cdot\mathbf{v}\,d\mathbf{x} + \int_\Omega \left(-p\mathbf{I} + \frac{1}{Re}(\nabla\mathbf{u})^T\right) : \nabla\mathbf{v}\,d\mathbf{x} = \int_P \boldsymbol{\lambda}\cdot\mathbf{v}\,d\mathbf{x} - \int_\Omega \frac{Gr}{Re^2}\overline{T}_f\frac{\mathbf{g}}{g}\cdot\mathbf{v}\,d\mathbf{x}, \tag{31}$$

$$\int_\Omega q\nabla\cdot\mathbf{u}\,d\mathbf{x} = 0, \tag{32}$$

$$(\rho_r - 1)\left[S_p^*\left(\frac{d\mathbf{U}}{dt} - Fr\frac{\mathbf{g}}{g}\right)\cdot\mathbf{V} + J^*\frac{d\boldsymbol{\omega}}{dt}\cdot\boldsymbol{\xi}\right] = -\int_P \boldsymbol{\lambda}\cdot(\mathbf{V} + \boldsymbol{\xi}\times\mathbf{r})\,d\mathbf{x} - \int_P (\rho_r\beta_r - 1)\frac{Gr}{Re^2}\overline{T}_f\frac{\mathbf{g}}{g}\cdot(\mathbf{V} + \boldsymbol{\xi}\times\mathbf{r})\,d\mathbf{x}, \tag{33}$$

$$\int_P [\mathbf{u} - (\mathbf{U} + \boldsymbol{\omega}\times\mathbf{r})]\cdot\boldsymbol{\zeta}\,d\mathbf{x} = 0, \tag{34}$$

in which p is the fluid pressure, and the following dimensionless parameters are introduced:

$$\text{density ratio}: \quad \rho_r = \frac{\rho_{s0}}{\rho_{f0}}, \tag{35}$$

$$\text{thermal expansion ratio}: \quad \beta_r = \frac{\beta_s}{\beta_f}, \tag{36}$$

$$\text{Grashof number}: \quad Gr = \frac{\rho_{f0}^2\beta_f L_c^3 g(T_m - T_0)}{\eta^2}, \tag{37}$$

$$\text{Reynolds number}: \quad Re = \frac{\rho_{f0}U_c L_c}{\eta}, \tag{38}$$

$$\text{Froude number}: \quad Fr = \frac{gL_c}{U_c^2}. \tag{39}$$

Here the Froude number represents the relative importance of gravity with respect to inertia, and η denotes the fluid viscosity. In (33), S_p^* and J^* are dimensionless particle area and moment of inertia, defined by $S_p^* = M/(\rho_s L_c^2)$ and $J^* = J/(\rho_s L_c^4)$. Note that these definitions are for the 2D case, and for the circular particle, $S_p^* = \pi(a^*)^2$ and $J^* = \frac{S_p^*(a^*)^2}{5}$, here a^* being the dimensionless particle radius. In (31), $(\nabla \mathbf{u})^T$ represents the transpose of the velocity gradient.

The combined temperature equations (14)–(16) can be non-dimensionalized as follows:

$$\int_\Omega \left(\frac{\partial \overline{T}_f}{\partial t} + \mathbf{u}\cdot\nabla\overline{T}_f - \overline{Q}_f\right)\Upsilon_f \,d\mathbf{x} + \int_\Omega \frac{1}{Pe}\nabla\overline{T}_f\cdot\nabla\Upsilon_f \,d\mathbf{x} = \int_P \lambda_T \Upsilon_f \,d\mathbf{x}, \tag{40}$$

$$\int_P [(\rho_r c_{pr} - 1)\frac{d\overline{T}_s}{dt} - (\overline{Q}_s - \overline{Q}_f)]\Upsilon_s \,d\mathbf{x} + \int_P (k_r - 1)\frac{1}{Pe}\nabla\overline{T}_s\cdot\nabla\Upsilon_s \,d\mathbf{x} = -\int_P \lambda_T \Upsilon_s \,d\mathbf{x}, \tag{41}$$

$$\int_P (\overline{T}_f - \overline{T}_s)\zeta_T \,d\mathbf{x} = 0, \tag{42}$$

where the following dimensionless quantities are introduced:

$$\text{specific heat ratio}: \quad c_{pr} = \frac{c_{ps}}{c_{pf}}, \tag{43}$$

$$\text{thermal conductivity ratio}: \quad k_r = \frac{k_s}{k_f}, \tag{44}$$

$$\text{Peclet number}: \quad Pe = \frac{\rho_f c_{pf} U_c L_c}{k_f}, \tag{45}$$

$$\text{dimensionless heat sources}: \quad \overline{Q}_f = \frac{Q_f L_c}{\rho_f c_{pf} U_c (T_m - T_0)}, \quad \overline{Q}_s = \frac{Q_s L_c}{\rho_f c_{pf} U_c (T_m - T_0)}. \tag{46}$$

Note that $Pe = Re\,Pr$ and $Ra = Gr\,Pr$, where Ra is the Rayleigh number and Pr is the Prandtl number defined by $Pr = \frac{\eta c_{pf}}{k_f}$.

The dimensionless equations for (19) and (20) are:

$$\int_\Omega \left(\frac{\partial \overline{T}_f}{\partial t} + \mathbf{u}\cdot\nabla\overline{T}_f - \overline{Q}_f\right)\Upsilon_f \,d\mathbf{x} + \int_\Omega \frac{1}{Pe}\nabla\overline{T}_f\cdot\nabla\Upsilon_f \,d\mathbf{x} = \int_P \lambda_T \Upsilon_f \,d\mathbf{x}, \tag{47}$$

$$\int_P (\overline{T}_f - \overline{T}_b)\zeta_T \,d\mathbf{x} = 0. \tag{48}$$

3. Computational scheme

3.1. Fractional step scheme for equations of motion

Following Glowinski et al. [4] and Yu [19], we employ the first-order accurate fractional step (or operator-splitting) scheme to decouple the system (31)–(34) into two sub-problems:

Fluid problem for $\mathbf{u}^*$ and p:

$$\int_\Omega \frac{\mathbf{u}^* - \mathbf{u}^n}{\Delta t}\cdot\mathbf{v}\,d\mathbf{x} + \int_\Omega \left[-p\mathbf{I} + \frac{(\nabla\mathbf{u}^*)^T + (\nabla\mathbf{u}^n)^T}{2Re}\right] : \nabla\mathbf{v}\,d\mathbf{x} = \int_\Omega \frac{1}{2}(3\mathbf{G}^n - \mathbf{G}^{n-1})\cdot\mathbf{v}\,d\mathbf{x} + \int_{P^n} \lambda^n\cdot\mathbf{v}\,d\mathbf{x}, \tag{49}$$

$$\int_\Omega q\nabla\cdot\mathbf{u}^*\,d\mathbf{x} = 0, \tag{50}$$

where $\mathbf{G} = -\mathbf{u}\cdot\nabla\mathbf{u} - \frac{Gr}{Re^2}\overline{T}_f\frac{\mathbf{g}}{g}$.

Particle problem for $\mathbf{U}^{n+1}$, $\boldsymbol{\omega}^{n+1}$, $\mathbf{u}^{n+1}$ and $\boldsymbol{\lambda}^{n+1}$:

$$\int_{\Omega}\left(\frac{\mathbf{u}^{n+1}-\mathbf{u}^{*}}{\Delta t}\right)\cdot\mathbf{v}\,\mathrm{d}\mathbf{x}=\int_{P^n}(\boldsymbol{\lambda}^{n+1}-\boldsymbol{\lambda}^{n})\cdot\mathbf{v}\,\mathrm{d}\mathbf{x}, \tag{51}$$

$$\begin{aligned}(\rho_{\mathrm{r}}-1)&\left[S_{\mathrm{p}}^{*}\left(\frac{\mathbf{U}^{n+1}-\mathbf{U}^{n}}{\Delta t}-Fr\frac{\mathbf{g}}{g}\right)\cdot\mathbf{V}+J^{*}\frac{\boldsymbol{\omega}^{n+1}-\boldsymbol{\omega}^{n}}{\Delta t}\cdot\boldsymbol{\xi}\right]\\&=-\int_{P^n}\boldsymbol{\lambda}^{n+1}\cdot(\mathbf{V}+\boldsymbol{\xi}\times\mathbf{r})\,\mathrm{d}\mathbf{x}-\int_{P^n}(\rho_{\mathrm{r}}\beta_{\mathrm{r}}-1)\frac{Gr}{Re^2}\left(\frac{3}{2}\overline{T}_{\mathrm{f}}^{n}-\frac{1}{2}\overline{T}_{\mathrm{f}}^{n-1}\right)\frac{\mathbf{g}}{g}\cdot(\mathbf{V}+\boldsymbol{\xi}\times\mathbf{r})\,\mathrm{d}\mathbf{x},\end{aligned} \tag{52}$$

$$\int_{P^n}\left[\mathbf{u}^{n+1}-(\mathbf{U}^{n+1}+\boldsymbol{\omega}^{n+1}\times\mathbf{r})\right]\cdot\boldsymbol{\zeta}\,\mathrm{d}\mathbf{x}=0. \tag{53}$$

One may set $\boldsymbol{\lambda}^{n}$ in (49) and (51) to be zero, as in Glowinski et al. [4], but we found that the presence of this term is helpful to reduce the error in the steady solution and allows one to use a significantly larger time step for low Reynolds flows.

3.1.1. Solution of fluid sub-problem

As proposed in [16], the finite-difference-based projection method on a half-staggered grid is used to solve the fluid sub-problem (49) and (50), where "half-staggered grid" means that the velocity components are collocated but the pressure nodes are staggered with the velocity nodes, the same pattern as "Q_1-P_0" finite-element scheme [40,15]. Because the fluid velocities need to be interpolated between the Eulerian and the Lagrangian frames in the resolution of the particle problem (51)–(53), the half-staggered scheme is simpler than the commonly used completely-staggered scheme, and furthermore our 2D tests for the square grid showed that the former provided solutions of a little better quality and exhibited no sign of deterioration in robustness compared to the latter.

The following projection scheme is used to further decouple (49) and (50) (assume Dirichlet boundary condition):

1. $$\frac{\mathbf{u}^{\#}-\mathbf{u}^{n}}{\Delta t}-\frac{1}{2Re}\nabla^2\mathbf{u}^{\#}=\frac{1}{2Re}\nabla^2\mathbf{u}^{n}-\nabla p^{n}+\boldsymbol{\lambda}_{P}^{n}+\frac{1}{2}(3\mathbf{G}^{n}-\mathbf{G}^{n-1}),\quad \mathbf{u}^{\#}=\mathbf{u}_{\Gamma}\ \text{on}\ \Gamma. \tag{54}$$

2. $$\nabla^2\phi=\frac{\nabla\cdot\mathbf{u}^{\#}}{\Delta t},\qquad \frac{\partial\phi}{\partial n}=0\quad\text{on}\ \Gamma. \tag{55}$$

3. $$\frac{\mathbf{u}^{*}-\mathbf{u}^{\#}}{\Delta t}=-\nabla\phi, \tag{56}$$

$$p^{n+1}=p^{n}+\phi. \tag{57}$$

In (54), $\boldsymbol{\lambda}_{P}^{n}$ represents

$$\boldsymbol{\lambda}_{P}^{n}=\frac{1}{h^2}\int_{P^n}\boldsymbol{\lambda}^{n}\cdot\mathbf{v}\,\mathrm{d}\mathbf{x}^{n}, \tag{58}$$

where h denotes the fluid mesh size, and $\mathbf{v}$ now represents the bi-linear interpolation function for the fluid nodes. The coefficient $\frac{1}{h^2}$ stems from the diagonal mass matrix $h^2\mathbf{I}$ of the finite-element scheme for the square grid, when reduced to the finite-difference scheme. The trapezoidal rule is used to integrate (58). It can be easily verified that replacing (57) with $p^{n+1}=p^{n}+\phi-\frac{\Delta t}{2Re}\nabla^2\phi$ yields an exactly second-order accurate scheme for the diffusion term [41], however, our tests showed that the effect of this modification on the results is always negligibly small. The time and space discretization schemes for the Lagrange multiplier terms were observed most crucial to the accuracy of our DLM/FD code.

Eq. (54) is a diffusion problem and can be further decomposed into two tri-diagonal systems with the ADI technique. We adopt the following version:

$$\frac{\mathbf{u}^{n+1/2}-\mathbf{u}^{n}}{\Delta t/2}=\frac{1}{Re}(\nabla_x^2\mathbf{u}^{n+1/2}+\nabla_y^2\mathbf{u}^{n})+\boldsymbol{\lambda}_P^n-\nabla p^n+\frac{1}{2}(3\mathbf{G}^n-\mathbf{G}^{n-1}),$$
$$\frac{\mathbf{u}^{\#}-\mathbf{u}^{n+1/2}}{\Delta t/2}=\frac{1}{Re}(\nabla_x^2\mathbf{u}^{n+1/2}+\nabla_y^2\mathbf{u}^{\#})+\boldsymbol{\lambda}_P^n-\nabla p^n+\frac{1}{2}(3\mathbf{G}^n-\mathbf{G}^{n-1}). \quad (59)$$

Eq. (55) is an elliptic problem on a staggered grid with a homogeneous Neumann boundary condition and can be efficiently solved by using a combination of a specialized fast cosine transformation (FCT) and a tri-diagonal system solver. The reader can find the codes of both FCT and a tri-diagonal system solver in Press et al. [42].

All derivatives in above equations are discretized with the central difference scheme.

3.1.2. Solution of particle sub-problem

The particle sub-problem (51)–(53) is a saddle-point problem and can be efficiently solved with the Uzawa conjugate gradient iterative method (Glowinski et al. [4]). The key issue is the spatial discretization of the Lagrange multiplier terms involving both Eulerian and Lagrangian quantities. The collocation-point method is the simplest and most efficient one, and has been widely used [4,16], however, we found that the calculated drag coefficient for the particle sedimenting in a bounded or periodic domain at low Reynolds numbers is always overestimated by a few percent if on the particle boundary the collocation points are also distributed. Höfler et al. [3] observed the same in their IB simulations and attributed this to the fact that the effective hydrodynamic radius of the particle is expected to be slightly larger than the geometrical radius of the reference point arrangement because each point controls a fluid volume reaching beyond its geometric location by $h/2$ in each direction. Therefore, one needs to retract the collocation points slightly from the particle geometric surface of prescribed radius in order to improve the accuracy. In the present study, the collocation-element method proposed by Yu et al. [15] is employed for its advantage that the above ad hoc adjustment of the particle radius is not required. The collocation-element method resembles the finite-element method with piecewise constant Lagrange multipliers on elements but differs in that it is a meshless method, which facilitates the construct of homogeneous discrete elements. Fig. 2 shows the element arrangement used in our collocation-element method: small circular elements with the center points distributed on concentric rings [15] and with the radius being slightly larger than the velocity mesh size for the good convergence rate of the Uzawa iteration [4]. The velocity of each element is obtained by averaging the velocities on the center point and the N points homogeneously located on the boundary with the center–boundary weight ratio of $N/2$ from the trapezoidal rule, and is then required to satisfy the rigid-body motion constraint. The velocities on the collocation points are determined from the bi-linear interpolation. The element arrangement shown in Fig. 2 differs from the one devised in [15] where some layers of boundary-fitted elements were used together with the inner meshless elements. The former is chosen here because it is simpler and produces almost equally accurate results; both errors in the calculated particle terminal settling velocities at low Reynolds numbers with the

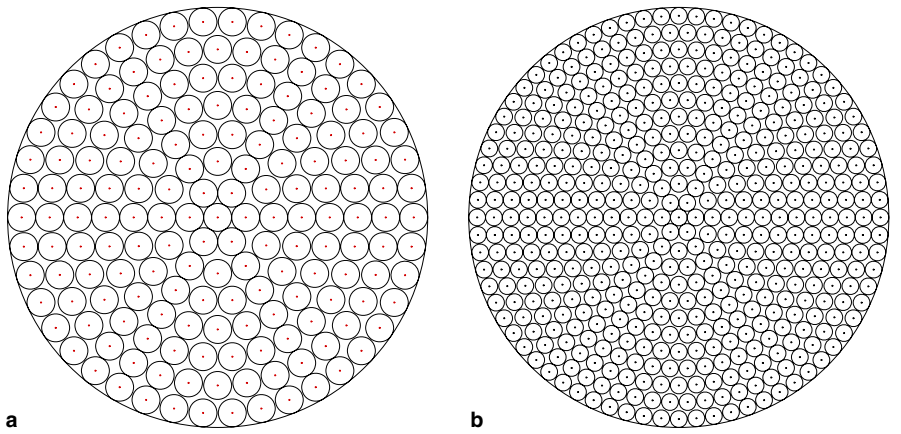

Fig. 2. Element arrangement in the collocation-element method for the Lagrange multiplier associated with the rigidity constraints: (a) typically used in association with the velocity mesh size of $h = a^*/8$, and (b) $h = a^*/16$, a^* being the dimensionless particle radius.

velocity mesh size of $h = a^*/8$ (a^* being the particle radius) for a fairly wide channel (e.g. $8a^*$ width) were observed within 1% compared to the analytical solution. Four points on each element boundary ($N = 4$) is enough for accuracy in the case of $h = a^*/8$, but the use of more points was observed beneficial to the improvement of smoothness in the particle velocity in case of coarse meshes (e.g. $h = a^*/4$).

3.2. Solution of temperature equations

3.2.1. The case of fixed temperature on the particle boundary

The fractional step scheme is also used to decouple the system (47) and (48) into two sub-problems: temperature problem for $\overline{T}_{\mathrm{f}}^{*}$:

$$\int_{\Omega}\left[\frac{\overline{T}_{\mathrm{f}}^{*}-\overline{T}_{\mathrm{f}}^{n}}{\Delta t}+\left(\frac{3}{2}\mathbf{u}^{n}\cdot\nabla\overline{T}_{\mathrm{f}}^{n}-\frac{1}{2}\mathbf{u}^{n-1}\cdot\nabla\overline{T}_{\mathrm{f}}^{n-1}\right)-\overline{Q}_{\mathrm{f}}\right]\Upsilon_{\mathrm{f}}\,\mathrm{d}\mathbf{x}+\int_{\Omega}\frac{1}{2Pe}(\nabla\overline{T}_{\mathrm{f}}^{*}+\nabla\overline{T}_{\mathrm{f}}^{n})\cdot\nabla\Upsilon_{\mathrm{f}}\,\mathrm{d}\mathbf{x}=\int_{\partial P^{n}}\lambda_{\mathrm{T}}^{n}\Upsilon_{\mathrm{f}}\,\mathrm{d}\mathbf{x} \tag{60}$$

and Lagrange multiplier problem for $\overline{T}_{\mathrm{f}}^{n+1}$ and $\lambda_{\mathrm{T}}T^{n+1}$:

$$\int_{\Omega}\left(\frac{\overline{T}_{\mathrm{f}}^{n+1}-\overline{T}_{\mathrm{f}}^{*}}{\Delta t}\right)\Upsilon_{\mathrm{f}}\,\mathrm{d}\mathbf{x}=\int_{\partial P^{n}}(\lambda_{\mathrm{T}}^{n+1}-\lambda_{\mathrm{T}}^{n})\Upsilon_{\mathrm{f}}\,\mathrm{d}\mathbf{x}, \tag{61}$$

$$\int_{\partial P^{n}}[\overline{T}_{\mathrm{f}}^{n+1}-\overline{T}_{\mathrm{b}}]\zeta_{\mathrm{T}}\,\mathrm{d}\mathbf{x}=0. \tag{62}$$

Following the schemes for the flow problem, we solve the temperature equation (60) with the finite-difference ADI method and the Lagrange multiplier problem (61) and (62) with the Uzawa iteration. The particle boundary is partitioned into 40 homogeneous line collocation elements for the case of $h = a^*/8$ and 80 for $h = a^*/16$. One center point and two end points are used to calculate the average velocity of the element with the center–end weight ratio of 2. The bi-linear interpolation function is also used for the temperature problems here and below.

3.2.2. The case of freely varying temperature on the particle boundary

The system (40)–(42) can be discretized in time with a fully implicit scheme as follows:

$$\begin{aligned}&\int_{\Omega}\left[\frac{\overline{T}_{\mathrm{f}}^{n+1}-\overline{T}_{\mathrm{f}}^{n}}{\Delta t}+\left(\frac{3}{2}\mathbf{u}^{n}\cdot\nabla\overline{T}_{\mathrm{f}}^{n}-\frac{1}{2}\mathbf{u}^{n-1}\cdot\nabla\overline{T}_{\mathrm{f}}^{n-1}\right)-\overline{Q}_{\mathrm{f}}\right]\Upsilon_{\mathrm{f}}\,\mathrm{d}\mathbf{x}\\&\quad+\int_{\Omega}\frac{1}{2Pe}(\nabla\overline{T}_{\mathrm{f}}^{n+1}+\nabla\overline{T}_{\mathrm{f}}^{n})\cdot\nabla\Upsilon_{\mathrm{f}}\,\mathrm{d}\mathbf{x}=\int_{P^{n}}\lambda_{\mathrm{T}}^{n+1}\Upsilon_{\mathrm{f}}\,\mathrm{d}\mathbf{x},\end{aligned} \tag{63}$$

$$\begin{aligned}&\int_{P^{n}}\left[(\rho_{\mathrm{r}}c_{\mathrm{pr}}-1)\frac{\overline{T}_{\mathrm{s}}^{n+1}-\overline{T}_{\mathrm{s}}^{n}}{\Delta t}-(\overline{Q}_{\mathrm{s}}-\overline{Q}_{\mathrm{f}})\right]\Upsilon_{\mathrm{s}}\,\mathrm{d}\mathbf{x}\\&\quad+\int_{P^{n}}\frac{(k_{\mathrm{r}}-1)}{2Pe}(\nabla\overline{T}_{\mathrm{s}}^{n+1}+\nabla\overline{T}_{\mathrm{s}}^{n})\cdot\nabla\Upsilon_{\mathrm{s}}\,\mathrm{d}\mathbf{x}=-\int_{P^{n}}\lambda_{\mathrm{T}}^{n+1}\Upsilon_{\mathrm{s}}\,\mathrm{d}\mathbf{x},\end{aligned} \tag{64}$$

$$\int_{P^{n}}(\overline{T}_{\mathrm{f}}^{n+1}-\overline{T}_{\mathrm{s}}^{n+1})\zeta_{\mathrm{T}}\,\mathrm{d}\mathbf{x}=0. \tag{65}$$

The solid temperature is solved in a Lagrangian frame, thus there is no convection term in (64). Regarding the space scheme, the left-hand side terms in (63) are discretized with the (central) finite-difference scheme, the left-hand side terms in (64) are discretized with the (bi-linear) finite-element scheme, and all other terms involving the Lagrange multiplier or its variance are discretized with a collocation-point-like method, which is resulted from taking the Lagrange multiplier space as $H^1(P)$ and using the trapezoidal rule to perform the integration on discrete solid elements. The collocation-point-like scheme resembles the collocation-point scheme in that the temperature constraint (65) is also satisfied point-by-point but differs in that the discrete product of the Lagrange multiplier and the temperature shape function is weighted with the support area of the solid temperature shape function. Apparently, the weights for the points on the boundary are smaller than those for inner points in case of homogeneous meshes, as compared to the same weight (unity) for all points in

the collocation-point method. Zero-weight for the boundary points means the elimination of these points, therefore, instead of retracting the collocation points from the boundary, one could also circumvent the drawback of the collocation-point method discussed earlier by reducing appropriately the relative weight for the points on the particle boundary, as also confirmed in our test problems of sedimentation.

The system (63)–(65) is a saddle-point problem and is solved with the Uzawa conjugate gradient method (Glowinski et al. [4]). In the Uzawa iteration, the fluid temperature sub-problem is solved with the conjugate gradient iteration and the solid temperature sub-problem is solved with the LU decomposition method [42]; note that the LU decomposition just needs to be done once. The iteration was found convergent for the case of $(\rho_r c_{pr} - 1)(k_r - 1) > 0$, but not for $(\rho_r c_{pr} - 1)(k_r - 1) < 0$, namely negative diffusion for the solid temperature sub-problem (64). The difficulty could be overcome by using other solvers, but we postpone the study to a future work. In the following, we present a very simple scheme for the solution of the temperature system (40)–(42), based on the fully explicit computation of the Lagrange multiplier. This simple scheme is not only much more efficient than the fully implicit scheme in the general case, but also works in case of $(\rho_r c_{pr} - 1)$-$(k_r - 1) < 0$, as long as both $(\rho_r c_{pr} - 1)$ and the time step are small.

Following the spirit of the IB method proposed by Peskin [18], we devise the simple scheme as follows: first solve the diffusion problem

$$\int_\Omega \left[\frac{\overline{T}_f^{n+1} - \overline{T}_f^n}{\Delta t} + \left(\frac{3}{2}\mathbf{u}^n \cdot \nabla \overline{T}_f^n - \frac{1}{2}\mathbf{u}^{n-1} \cdot \nabla \overline{T}_f^{n-1}\right) - \overline{Q}_f\right] \Upsilon_f \, d\mathbf{x} + \int_\Omega \frac{1}{2Pe}(\nabla \overline{T}_f^{n+1} + \nabla \overline{T}_f^n) \cdot \nabla \Upsilon_f \, d\mathbf{x} = \int_{P^n} \lambda_T^n \Upsilon_f \, d\mathbf{x}, \tag{66}$$

then set $\overline{T}_s^{n+1} = \overline{T}_f^{n+1}$ at the collocation points via the bi-linear interpolation, and finally explicitly calculate the Lagrange multiplier with the following equation:

$$-\int_{P^n} \lambda_T^{n+1} \Upsilon_s \, d\mathbf{x} = \int_{P^n} \left[(\rho_r c_{pr} - 1)\frac{\overline{T}_s^{n+1} - \overline{T}_s^n}{\Delta t} - (\overline{Q}_s - \overline{Q}_f)\right] \Upsilon_s \, d\mathbf{x} + \int_{P^n} \frac{(k_r - 1)}{2Pe}(\nabla \overline{T}_s^{n+1} + \nabla \overline{T}_s^n) \cdot \nabla \Upsilon_s \, d\mathbf{x}. \tag{67}$$

The space discretization schemes for (66) and (67) are the same as used in the fully implicit scheme discussed above. Eq. (66) can be also solved with the ADI approach.

The validation and discussion on the simple scheme will be presented later. Fig. 3 shows three meshes tested in this study for the solid temperature. The size of any individual solid element being larger than the fluid mesh size ensures a good convergence rate in the Uzawa iteration (typically less than 5 iterations).

3.3. Collision model

Before concluding this section, we briefly describe our updated collision strategy. The collision models for the particulate flows can be classified into two categories: binary hard-sphere model and soft-sphere model [43]. For the hard-sphere model, the momentum exchange between two colliding particles takes place exactly at the time when the two particles touch and the post-collision velocities of the particles are determined from

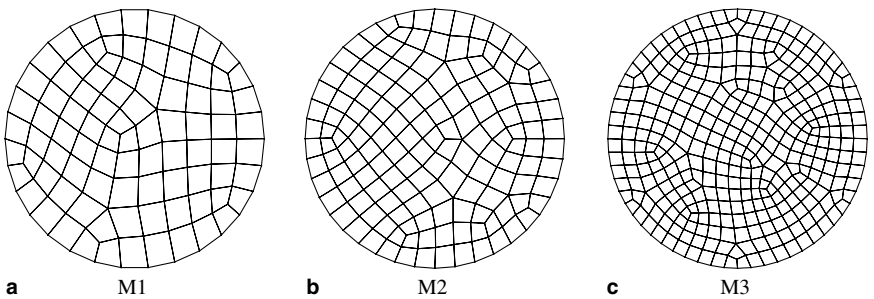

Fig. 3. Three meshes for the solid temperature. M1 has 88 elements and 104 nodes, M2 has 145 elements and 166 nodes, and M3 has 333 elements and 364 nodes. M1 and M2 are used with the fluid mesh $h = a^*/8$ and M3 is used with $h = a^*/16$, a^* being the particle radius.

the system momentum conservation and energy conservation or loss (elastic or inelastic collision). In contrast, for the soft-sphere model, the velocities of colliding particles are determined from the Newton's equation of motion with the collision forces of soft-potential as a function of the separation or overlap distances between the particles and possibly the particle velocities. The behavior of particles in a non-concentrated suspension is mainly controlled by the long-range hydrodynamic interactions and is insignificantly affected by the short-range interactions [44]. Therefore, one can choose any collision model primarily for numerical convenience. A soft-sphere model with an artificial repulsive force was developed by Glowinski et al. [4] and was later used by Yu et al. [15] in the DLM/FD simulations. An inconvenience in this model is that one needs to adjust the intensity of the repulsive force in order to ensure that the colliding particles neither overlap nor rebound too much. We have substituted the analytical lubrication force for the artificial repulsive force in our DLM/FD code.

We first split the Newton's equation of motion

$$M\frac{\mathrm{d}\mathbf{U}}{\mathrm{d}t} = \mathbf{F}^{\mathrm{l}} + \mathbf{F}^{\mathrm{s}} \tag{68}$$

into

$$M\frac{\mathbf{U}^{*} - \mathbf{U}^{n}}{\Delta t} = \mathbf{F}^{\mathrm{l}} \tag{69}$$

and

$$M\frac{\mathbf{U}^{n+1} - \mathbf{U}^{*}}{\Delta t} = \mathbf{F}^{\mathrm{s}}, \tag{70}$$

where $\mathbf{F}^{\mathrm{l}}$ denotes the long-range force on the particles that is not sensitive to the slight change in the particle configuration and $\mathbf{F}^{\mathrm{s}}$ denotes the short-range force. For simplicity of exposition, we only consider the translational equation, or one can consider that the above equations also include the angular components. From (21), one can get the hydrodynamic force on the rigid particle $\mathbf{F}^{\mathrm{H}} = -\int_P \boldsymbol{\lambda}\,\mathrm{d}\mathbf{x} + \frac{M}{\rho_{\mathrm{r}}}\frac{\mathrm{d}\mathbf{U}}{\mathrm{d}t}$. If we assume that the Lagrange multiplier is only used to determine the long-range hydrodynamic force and does not depend on the short-range force, we can define the long-range hydrodynamic force $\mathbf{F}^{\mathrm{lH}} = -\int_P \boldsymbol{\lambda}\,\mathrm{d}\mathbf{x} + \frac{M}{\rho_{\mathrm{r}}}\frac{\mathbf{U}^{*}-\mathbf{U}^{n}}{\Delta t}$ and deduce (23) from (69). In the previous DLM/FD works [4,15], because the Lagrange multiplier is not independent of the short-range force via $\mathbf{F}^{\mathrm{lH}} = -\int_P \boldsymbol{\lambda}\,\mathrm{d}\mathbf{x} + \frac{M}{\rho_{\mathrm{r}}}\frac{\mathbf{U}^{n+1}-\mathbf{U}^{n}}{\Delta t}$, the operator splitting of (68) with the Lagrange multiplier being substituted in gives (23) and

$$\left(1 - \frac{1}{\rho_{\mathrm{r}}}\right)M\frac{\mathbf{U}^{n+1} - \mathbf{U}^{*}}{\Delta t} = \mathbf{F}^{\mathrm{s}} \tag{71}$$

instead of (70). Since the artificial short-range force is adjusted for the numerical convenience, the coefficient $(1 - \frac{1}{\rho_{\mathrm{r}}})$ does not matter, but in case of a physical short-range force we prefer (70) because we believe that it is more physical and it avoids the singularity at $\rho_{\mathrm{r}} = 1$ in (71).

In the case of relatively low Reynolds numbers, we have incorporated the lubrication force in our code by adopting and modifying the ASD code [5]. Eq. (70) is rewritten as follows:

$$M\frac{\mathbf{U}^{n+1} - \mathbf{U}^{*}}{\Delta t} = \mathbf{F}^{\mathrm{sH}} + \mathbf{F}^{\mathrm{sP}}, \tag{72}$$

where $\mathbf{F}^{\mathrm{sH}}$ represents the short-range hydrodynamic force, namely the lubrication force, which is expressed as

$$\mathbf{F}^{\mathrm{sH}} = -[\mathbf{R}(\mathbf{r}) - \mathbf{R}(\mathbf{r}_0)] \cdot \mathbf{U}, \tag{73}$$

here $\mathbf{R}$ being the resistance matrix, $\mathbf{r}$ the connectors between particles, $\mathbf{r}_0 = r_0\frac{\mathbf{r}}{|\mathbf{r}|}$ so that the lubrication force correction vanishes at the cut-off distance r_0 [45], $\mathbf{U}$ the vector of particle velocities (including the angular velocities), and $\mathbf{F}^{\mathrm{sP}}$ denotes a short-range repulsive force with a very small range [5]. From the theoretical point of view, the lubrication force alone can prevent the particle overlap since the force diverges when two particles touch each other. However, the particle overlap can take place in the numerical simulations due to the fact that a finite time-step is used for the calculation of the particle trajectories. In fact, for relatively concentrated

suspensions, the numerical overlap between particles is unavoidable even if the repulsive force is added. As in the ASD code, when the overlap is detected, we set the inter-particle distance between overlapping particles to be $10^{-8}a^*$ for the calculation of the forces while keeping the particle positions unchanged. The repulsive force will drive the overlapping particles to move apart, and the simulation would be terminated if the overlapping distance is found to exceed $0.05a^*$. In the present study, the cut-off distance for the lubrication force $\mathbf{F}^{sH}$ is set to be the fluid mesh size and that for the repulsive force $\mathbf{F}^{sP}$ is $10^{-3}a^*$.

One can find the expressions of the full resistance matrices for the two-sphere [46] and sphere-wall problems [47]. For the 2D circular particle, only the most singular component due to the squeezing flow is normally considered in the literature. We take the form from [48] for this component and use the sphere counterparts for all other components from the numerical convenience point of view. Eq. (72) is implicitly solved with an efficient incomplete Choleski conjugate gradient method; the reader is referred to [5] for the discussion of this solver, and [49] for the expression of $\mathbf{F}^{sP}$ and its effect on the rheology of concentrated suspensions.

4. Numerical experiments and discussions

We first verify our method for the case of fixed temperature on the boundary by comparing our results on the natural convection driven by a hot cylinder placed eccentrically in a square enclosure and the sedimentation of a cold particle in a vertical channel to the data available in the literature. For the case of freely varying temperature on the boundary, we show that the method is able to produce mesh-size and time-step convergent results in a test problem: motion of a catalyst particle in an enclosed box. Finally, the method is applied to the preliminary analysis of the heat conductivity of nanofluids and sheared non-Brownian suspensions, respectively. Throughout the study, the heat source in the fluids is not considered, i.e., $\overline{Q}_f = 0$.

4.1. Case of both fixed velocity and temperature on the boundary: cylinder placed eccentrically in a square enclosure

Fig. 4 shows the schematic diagram of our first test problem: a natural thermal convection driven by a hot cylinder placed eccentrically in an enclosed square. We take the edge length of the square as the characteristic length. The dimensionless diameter of the cylinder $d = 0.4$, and the eccentric distance $\varepsilon = 0.1$. The dimensionless temperature is unity on the cylinder surface and vanishes on two side walls. The horizontal walls are adiabatic.

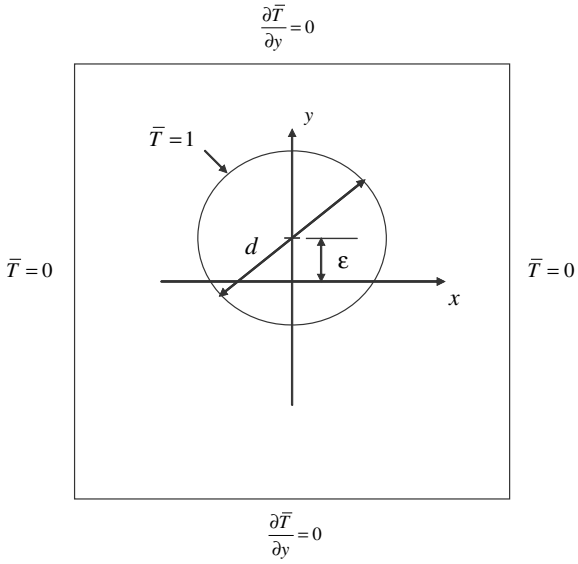

Fig. 4. Schematic diagram of a natural thermal convection problem arising from a hot cylinder placed eccentrically in an enclosed square.

The governing equations for the temperature are (47) and (48), and for the flow are (31), (32) and (34) with $\mathbf{U} = \boldsymbol{\omega} = 0$. Therefore, we actually use a boundary Lagrange multiplier for the temperature and a body Lagrange multiplier for the flow. We believe that the boundary Lagrange multiplier is better than the body one for the case of the Dirichlet condition on the boundary because the former is not only more efficient due to fewer degrees of freedom, but more accurate since the boundary condition is better satisfied. We choose the body Lagrange multiplier for the flow problem here just for a convenience that we can use the same code as for freely moving particles. The computed local Nusselt numbers (i.e., dimensionless temperature normal derivative on the boundary) along the side wall at $Re = 0.1$, $Pe = 1$ and $Gr = 10^5$ are plotted in Fig. 5 and compared to the benchmark results of Demirdžić et al. [50]. We see an excellent agreement between the two results.

4.2. Case of fixed temperature on the boundary of a freely moving particle: sedimentation of a cold particle in a vertical channel

Gan et al. [36] simulated the sedimentation of particles in a vertical channel with thermal convection using the ALE finite-element method, and the results for a cold particle settling in a channel of $8a^*$ width were presented and analyzed in full detail, providing a good test problem to verify our method. Gan et al. summarized some features of their method as the following. An unstructured mesh of triangular elements is generated by the Delaunay–Voronoi method. As the particles move, the mesh moves and deforms according to a 'mesh velocity' determined by a Laplace equation. When the elements become severely distorted, a remeshing and projection procedure is carried out to restore mesh quality. When a particle approaches another particle or a wall, the local mesh is automatically refined. Such a boundary-fitted method is supposed to be more accurate than our stationary-grid-based method for the simulation of motion of individual particles, but for the case of suspensions of multiple-particles, the frequently required remeshing and projection leads to a significant increase in the computational cost and the deterioration of accuracy. Due to the use of fixed mesh, our method is easy to implement and the parallelization of the code is simple. Therefore, our method is suited to a large-scale simulation of particulate flows. In addition, the method of Gan et al. has not been extended to the case of freely varying temperature on the particle boundaries.

Following Yu et al. [15], for the case of relatively strong inertial effect we define the characteristic velocity as

$$U_c = \sqrt{\pi a(\rho_r - 1)g}, \tag{74}$$

so that one can conveniently obtain the standard drag coefficient C_d from $C_d = 1/(U_T^*)^2$, here a being the particle radius, and U_T^* the computed dimensionless terminal settling velocity. Another advantage of this non-dimensionalization scheme is that U_T^* is always not far away from unity. The Froude number (39) becomes

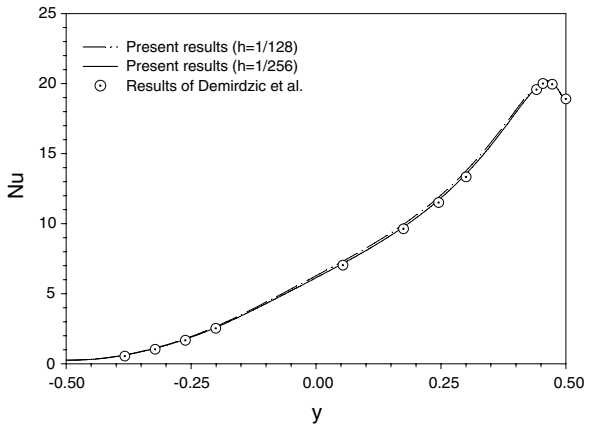

Fig. 5. Comparison between Demirdžić et al. [50] and our results on the local Nusselt number along the side wall for the cylinder placed eccentrically in a square enclosure.

$$Fr = \frac{1}{\pi a^*(\rho_r - 1)}. \tag{75}$$

We take the particle diameter as the characteristic length, so $a^* = 1/2$.

Since the interior solid temperature is not considered in the present case, it is not possible (or not necessary) to evaluate its effect on the buoyant force on the particle. Indeed, Gan et al. did not consider this effect, therefore, we set β_r to be zero in (33). The dimensionless physical parameter group comprises ρ_r, Gr, Re and Pr. As in Gan et al., we set $\rho_r = 1.00232$ and $Pr = 0.7$. Gan et al. did not report sufficient physical parameters that allow us to compute the exact value of Re, but they mentioned that the Reynolds number based on the terminal settling velocity Re_T at zero Gr is 21. Note that $Re_T = ReU_T^*$. Our tests showed that Re being 40.5 with other parameters given above yields a value of 21.2 for Re_T. The difference in Re_T is small, so we let Re be 40.5. The dimensionless temperature is unity on the particle boundary and zero on the side walls; then a cold particle implies a negative Grashof number, but we will refer to its magnitude below. The computational channel has width of 4 and height of 32. To mimic an infinitely high channel, we shift the flow fields and the particle position upwards one mesh distance once the particle falls below a vertical position that is 8 higher than the bottom inlet so that the channel looks like moving with the particle [15,16]. The initial velocities of the particle and fluids and the initial temperature are zero. In the following, we present the results for different Grashof numbers obtained with $h = 1/32$ and $\Delta t = 0.005$, and compare to those of Gan et al.

Gan et al. established five Gr regimes according to the particle lateral equilibrium positions and the wake structures as follows:

- Regime A ($0 < Gr < 500$): The particle settles steadily along the centerline and the wake vortices are steady and symmetric.
- Regime B ($500 < Gr < 810$): Vortices shed from the particle and the particle oscillates regularly about the channel centerline.
- Regime C ($810 < Gr < 2150$): The particle achieves steady-state settling close to one of the walls and there is no vortex shedding at the steady-state.
- Regime D ($2150 < Gr < 4500$): The centerline becomes once again a stable equilibrium position and vortex shedding remains absent.
- Regime E ($Gr > 4500$): The regime is characterized by the re-emergence of lateral oscillations about the centerline, and the authors attributed this to the roll-up of shear layers in the wake due to Kelvin–Helmholtz instability.

In the simulations of Gan et al., the particles were released at the centerline, which has a drawback that the trajectories in case of particle migrating away from the centerline are not deterministic since the migrations depend on the random numerical disturbances. We here release the particles at a lateral position being one particle radius away from the centerline. Figs. 6 and 7 show the vorticity contours and the evolutions of lateral particle positions at different Grashof numbers, respectively, and we see that the features of all regimes described above are well reproduced in our simulations. Gan et al. observed two types of migrations in Regime C: one with oscillation as a natural extension of Regime B, and the other without oscillation. Both are also reproduced in Fig. 7, and we found that the wake structure is responsible for the difference: for the former the wake vortices are attached to the particle, whereas for the latter at least one branch of the wake structures is detached from the particle, as shown in Fig. 6c. The alternating vortex shedding (or roll-up as observed by Gan et al.) from the detached wake structures at $Gr = 4000$ (Fig. 6e) does not affect the particle's motion as much as from the attached ones at $Gr = 564$ (Fig. 6b) because of much stronger confinement effects on the particle motion imposed by the detached circulations on both sides of the particle in the former case (Fig. 6e); the oscillation in the lateral position for $Gr = 4000$ is so small that it is indiscernible if plotted in Fig. 7. The particle lateral equilibrium position at $Gr = 2000$ is around 0.75 away from the centerline and agrees well with the result of Gan et al.

Despite good agreement for $Gr < 4000$, the two results differ significantly at high Grashof numbers. Our results at $Gr = 4000$ exhibit the feature of Regime E, resembling their results at $Gr = 5000$, rather than Regime

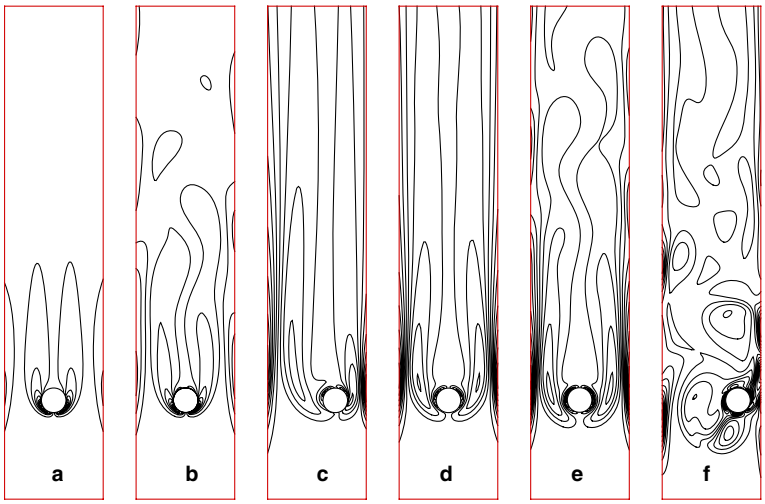

Fig. 6. Vorticity contours for a cold circular particle settling in a vertical channel of 4 particle diameter width at different Grashof numbers: (a) $Gr = 100$; (b) $Gr = 564$: (c) $Gr = 2000$; (d) $Gr = 2500$; (e) $Gr = 4000$; (f) $Gr = 4500$. $(\rho_r, Re, Pr) = (1.00232, 40.5, 0.7)$.

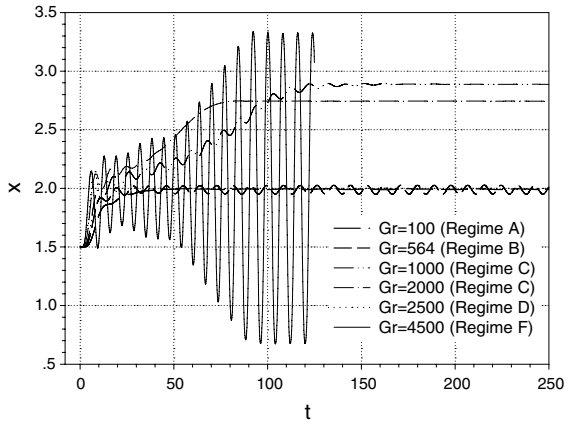

Fig. 7. Time development of lateral positions of a cold circular particle settling in a vertical channel of 4 particle diameter width at different Grashof numbers. The centerline is located at $x = 2$. $(\rho_r, Re, Pr) = (1.00232, 40.5, 0.7)$.

D as specified above. At $Gr = 4500$, our flow becomes turbulence-like (Fig. 6f) and the particle oscillates violently but still regularly (Fig. 7), a new regime that was not detected by Gan et al. and we term Regime F here. The reason for the discrepancies is not clear, however, it could be due to the fact that one normally uses a fine mesh only for the region in the vicinity of the particle boundary in the ALE method, but a fine mesh for the far-field region is probably also required to accurately predict the far-field instability at $Gr = 4000$ (Fig. 6e) and the strong global instability at $Gr = 4500$ (Fig. 6f). We have used a homogeneously fine mesh and ensured that our results are mesh-size and time-step independent.

Fig. 8 shows the comparison between the results of terminal-settling-velocity based Reynolds number Re_T at different Grashof numbers. Good agreement can be seen, particularly if considering the difficulty of the problem caused by the competition between the forced and natural thermal convections and the strong wall confinement, as reflected in the complex behavior of the curves in Fig. 8. In addition, as mentioned earlier, we were not able to exactly match Re to Gan et al.', and our Re being 40.5 results in a slightly larger Re_T of 21.2 compared to Gan et al.'s 21 at zero Grashof number, a probable reason why our Re_T are systematically higher than Gan et al.'s at all Grashof numbers, as shown in Fig. 8.

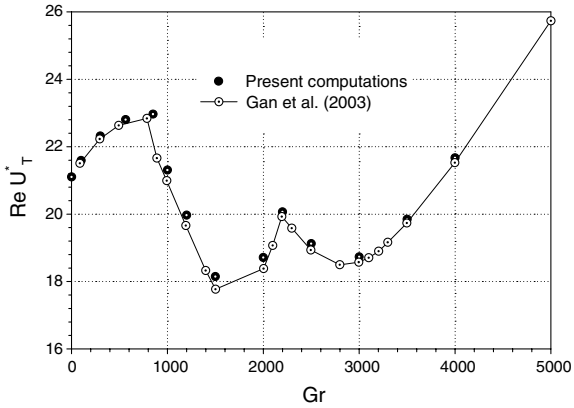

Fig. 8. Comparison of terminal-settling-velocity based Reynolds number Re_T at different Grashof numbers for a cold circular particle settling in a vertical channel of 4 particle diameter width.

4.3. Case of freely varying temperature on the boundaries of freely moving particles

4.3.1. Motion of a catalyst particle in a box

We now consider the motion of a catalyst particle in a box with an assumption that the heat is generated homogeneously inside the particle. The governing equations are (31)–(34) for the flow and (40)–(42) for the temperature. The dimensionless physical parameter group is $(Re, Gr, \rho_r, k_r, c_{pr}, \beta_r)$. The same non-dimensionalization scheme as for the cold particle problem above is used here. We set $Re = 40$, $Gr = 1000$ and $\beta_r = 0$. The enclosed box has width of 8 and height of 16. At the initial time, all velocities and the temperature are zero, and the particle is placed at the center of the box. We let $\overline{Q}_s = 1$.

We have presented two schemes for the current problem: one is the coupled scheme based on the fully implicit calculation of the Lagrange multiplier (63)–(65) and the other is the simple scheme based on the fully explicit calculation of the Lagrange multiplier (66) and (67). Fig. 9 shows that the results obtained with the two schemes for both sets of parameters $(\rho_r, k_r, c_{pr}) = (1.1, 15, 1)$ and $(1.6, 5, 1)$ are in perfect agreement with each other, indicating that the simple scheme is as accurate as the coupled scheme. However, the simple scheme is found only applicable to small $(\rho_r c_{pr} - 1)$; for example, when we changed (ρ_r, k_r, c_{pr}) from

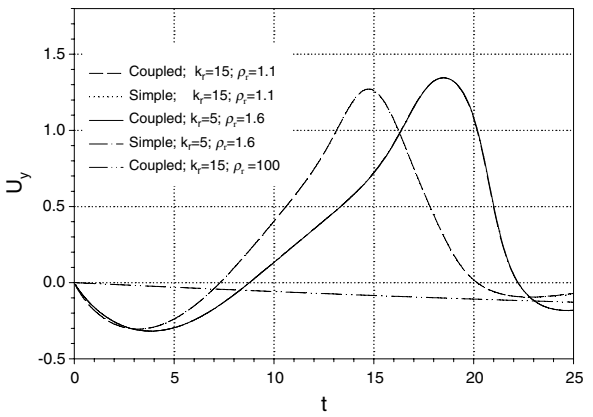

Fig. 9. Comparison of the evolutions of vertical velocities for a catalyst particle in an enclosed box obtained with the coupled scheme based on the fully implicit calculation of the Lagrange multiplier and the simple scheme based on the fully explicit calculation of the Lagrange multiplier, respectively. $Re = 40$, $Gr = 1000$, $c_{pr} = 1$, $\beta_r = 0$ and $\overline{Q}_s = 1$. The results show that the two schemes are equally accurate. The result for $\rho_r = 100$ is also plotted in order to show that the large density ratio does not pose the difficulty for the coupled scheme, although it does for the simple scheme.

$(1.6, 5, 1)$ to $(1.8, 5, 1)$, the computation was not stable, regardless of the value of the time step. For the case of large $(\rho_r c_{pr} - 1)$, one therefore needs to treat implicitly the unsteady term of the solid temperature equation. The coupled scheme is a candidate, and Fig. 9 confirms that it is stable at $\rho_r = 100$. The intermediate scheme based on the splitting of the Lagrange multiplier as we do for the flow problem is expected to work. In addition, one could follow the methods for the droplet (or bubble) problem [51,52] and solve a unified set of temperature equations with different coefficients for the fluids and solid; similar approach has been implemented in the IB method for fluid–structure interactions at non-unity density ratios [53]. The problem due to large k_r in the simple scheme is not as serious, and we found that its stability criterion is analogous to the one of the explicit scheme for the convection–diffusion equation, which is not surprising since both the diffusion term of the solid temperature equation and the convection term in the fluid equation are indeed treated explicitly in the simple scheme. Thus, for large k_r, the computation is stable as long as the time step is small enough, which normally is not a serious problem since a small time step is also required by the dynamic simulation method. Since we found that the code of the simple scheme runs faster than the one of the coupled scheme by typically a factor of 7 for the same time-step, the simple scheme is used for all computations below.

The mesh-size and time-step convergence tests are performed at $(\rho_r, k_r, c_{pr}) = (1.1, 5, 1)$, and it can be seen from Fig. 10a that the results are essentially independent of the meshes and time-steps used. As a result, we choose the coarsest mesh M1 for all other computations in this study, unless otherwise specified. As mentioned earlier, the coupled scheme with the Uzawa iteration fails at $(\rho_r c_{pr} - 1)(k_r - 1) < 0$, whereas the results presented in Fig. 10b demonstrate that the simple scheme still works in such a case.

Fig. 11 shows the isotherms and flow fields at different times for $(\rho_r, k_r, c_{pr}) = (1.1, 5.0, 1.0)$. At early stage, the effect of the temperature on the flow is small and the particle falls downwards. With more and more heats being generated inside the particle, a pair of buoyance-induced circulations have appeared by $t = 5$ (Fig. 11a) and dominated the flow by $t = 15$ (Fig. 11b), leading the particle to rise up. Finally, the wall confinement stops the particle from rising; from Fig. 10 we see that the particle vertical velocity almost vanishes at $t = 20$. Note that this is not caused by the direct touch of the particle with the wall, but the suppression of natural convection near the particle (Fig. 11c). The natural convection is more severely inhibited at the upper side of the particle than at the bottom side and consequently we can see worse heat removal at the upper side than at the bottom side (Fig. 11c).

If keeping other parameters unchanged, a reduction in c_{pr} leads to a more rapid increase in the solid temperature, and an enhancement in k_r causes more rapid heat transfer from the solid bulk region to the boundary and then to the fluids. Therefore, not surprisingly in Fig. 10b we see that the particle starts to rise earlier at smaller c_{pr} or larger k_r. The density ratio ρ_r plays the same role as c_{pr} in the solid temperature equation, but it also influences the particle inertia; the dimensionless velocity of a particle with large ρ_r changes very slowly with time, as illustrated in Fig. 9 for $\rho_r = 100$.

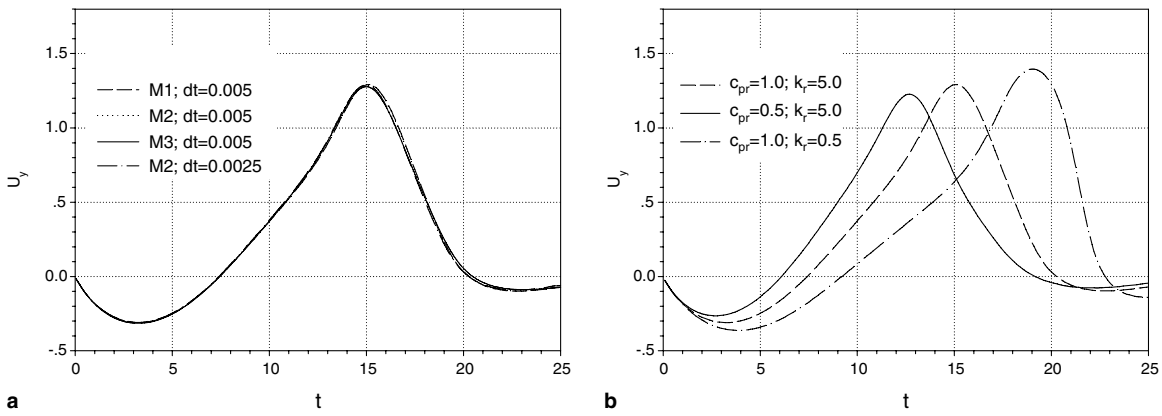

Fig. 10. (a) Evolutions of the vertical velocities of a catalyst particle computed with the simple scheme at different mesh-sizes and time-steps, showing that our results are convergent with mesh-size and time-step; (b) at different specific heat ratios and heat conductivity ratios, showing that the simple scheme works for $(\rho_r c_{pr} - 1)(k_r - 1) < 0$.

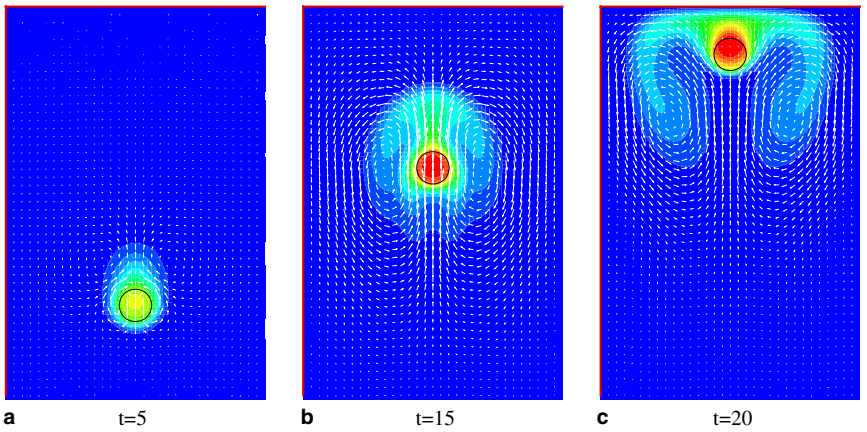

Fig. 11. Isotherms and velocity vectors for a catalyst particle in an enclosed box at different times. $(Re, Gr, \rho_r, k_r, c_{pr}, \beta_r) = (40, 1000, 1.1, 5.0, 1.0, 0.0)$.

4.3.2. Heat conductivity of suspensions

The heat conductivity of suspensions can be measured with a plate system, whose schematic diagram in two-dimensions is given in Fig. 12. The heat is inputted into the system through the top plate, resulting in a bulk temperature gradient across the suspension at steady-state that is defined by $\nabla_b T = \frac{(T_2 - T_1)}{H}$. From the Fourier law, the effective (or bulk) heat conductivity of the suspension k_e is determined from [54]

$$k_e = \frac{-\langle q_y \rangle_{\Gamma_2}}{\nabla_b T}, \tag{76}$$

here $-\langle q_y \rangle_{\Gamma_2}$ being the average input heat flux on the top plate. The micro-thermal-convection in the fluids induced by the Brownian motion of the nanoparticles has been regarded as a mechanism to explain the unusually high k_e of the nanofluids [34,33]. Following the Batchelor's derivation for the bulk viscosity of the suspension [55], one can obtain the contribution of the micro-convection to the effective heat conductivity or any effective macroscopic transport coefficient easily [56,57]. Consider a unified temperature equation

$$\rho c_p \frac{dT}{dt} = -\nabla \cdot \mathbf{q} + Q \tag{77}$$

with corresponding physical quantities for the solid and fluid domains, where $\mathbf{q}$ is the heat flux. Multiplying y to all terms in (77), integrating the resulting unsteady and source terms over the entire domain and integrating the heat flux term in part, we get

$$\frac{\int_{\Gamma_2}(-q_y)\,dx}{L} = \frac{1}{S}\left[\int_\Omega -q_y\,d\mathbf{x} + \int_\Omega y\left(\rho c_p \frac{dT}{dt} - Q\right) d\mathbf{x}\right], \tag{78}$$

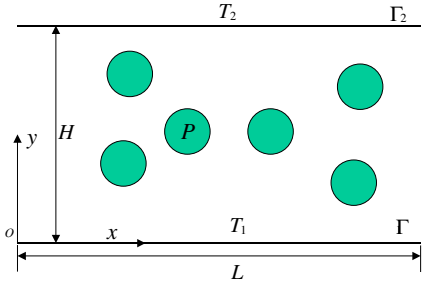

Fig. 12. Schematic diagram of a 2D plate system measuring the effective heat conductivity of suspensions. A bulk temperature gradient is imposed to the system in the y-direction, which is defined by $\nabla_b T = \frac{(T_2 - T_1)}{H}$. A periodic boundary condition is imposed in the x-direction in our computations.

where q_y is the heat flux in the y-direction, L the length of the cell, and S the area of the cell. As shown in Fig. 12, we place the bottom plate at $y = 0$, thus the boundary integral on this plate vanishes. For homogeneous suspensions, (78) holds irrespective of the definition of the coordinate origin, since the average output heat flux on the bottom plate should equal the input one on the top plate and the sum of the two terms again yields the left-hand side term in (78), i.e., the average input heat flux through the top plate. One can easily verify the following derivation:

$$\frac{1}{S}\int_{\Omega} -q_y \,\mathrm{d}\mathbf{x} = \frac{1}{S}\left[\int_{\Omega_\mathrm{f}} k_\mathrm{f}\nabla_y T_\mathrm{f}\,\mathrm{d}\mathbf{x} + \int_P k_\mathrm{s}\nabla_y T_\mathrm{s}\,\mathrm{d}\mathbf{x}\right] = \left[\frac{k_\mathrm{f}(T_2 - T_1)}{H} + \frac{1}{S}\sum_{i=1}^{N}\int_{\partial P_i}(k_\mathrm{s} - k_\mathrm{f})n_y T_\mathrm{s}\,\mathrm{d}x\right], \tag{79}$$

in which P_i denoted the solid domain of the ith particle among the total N particles and Ω_f the fluid domain. Without considering the heat source term, we can write the effective heat conductivity k_e as a sum of the molecular-heat-diffusion-related conductivity k_d (sometimes referred to as diffusion-related conductivity below) and the convection-induced conductivity k_c:

$$k_\mathrm{e} = k_\mathrm{d} + k_\mathrm{c}; \tag{80}$$

$$\frac{k_\mathrm{d}}{k_\mathrm{f}} = 1 + c\phi, \quad c = \frac{(k_\mathrm{r} - 1)}{NS_\mathrm{p}(\nabla_\mathrm{b} T)}\sum_{i=1}^{N}\int_{\partial P_i} n_y T_\mathrm{s}\,\mathrm{d}x; \tag{81}$$

$$\frac{k_\mathrm{c}}{k_\mathrm{f}} = \frac{\rho_\mathrm{f} c_\mathrm{pf}}{k_\mathrm{f}(\nabla_\mathrm{b} T)S}\left[\int_{\Omega_\mathrm{f}} y\frac{\mathrm{d}T_\mathrm{f}}{\mathrm{d}t}\,\mathrm{d}\mathbf{x} + \rho_\mathrm{r} c_\mathrm{pr}\int_P y\frac{\mathrm{d}T_\mathrm{s}}{\mathrm{d}t}\,\mathrm{d}\mathbf{x}\right]. \tag{82}$$

In (81), S_p and ϕ are the particle area and area fraction, respectively, and simply replacing them with the particle volume and volume fraction makes the above equations hold for the 3D case. Batchelor considered the contribution of the Reynolds stress in the bulk viscosity of the suspension [55]. As an analogue, the Reynolds-stress-type micro-convection term for the present problem has the form of $\frac{-\rho_\mathrm{f}}{S}[\int_{\Omega_\mathrm{f}} u_y' T_\mathrm{f}'\,\mathrm{d}\mathbf{x} + \rho_\mathrm{r}\int_P u_y' T_\mathrm{s}'\,\mathrm{d}\mathbf{x}]$, here u_y' being the fluctuating velocity in the y-direction and T_f' the fluctuating temperature. However, from the above derivation, this Reynolds-stress-type micro-convection term does not contribute to the effective heat conductivity of the suspension measured with the plate system (76), although it might play a role for the other measuring systems such as the hot-wire system [58].

Taking the particle diameter d as the characteristic length and defining the dimensionless temperature by $\overline{T} = \frac{H}{\mathrm{d}}\frac{T - T_1}{T_2 - T_1}$, we get:

$$\frac{k_\mathrm{e}}{k_\mathrm{f}} = \left\langle\frac{\partial\overline{T}_\mathrm{f}}{\partial y}\right\rangle_{\Gamma_2}, \tag{83}$$

$$c = \frac{4(k_\mathrm{r} - 1)}{N\pi}\sum_{i=1}^{N}\int_{\partial P_i} n_y\overline{T}_\mathrm{s}\,\mathrm{d}x, \tag{84}$$

$$\frac{k_\mathrm{c}}{k_\mathrm{f}} = \frac{Pe}{S^*}\left[\int_{\Omega_\mathrm{f}} y\frac{\mathrm{d}\overline{T}_\mathrm{f}}{\mathrm{d}t}\,\mathrm{d}\mathbf{x} + \rho_\mathrm{r} c_\mathrm{pr}\int_P y\frac{\mathrm{d}\overline{T}_\mathrm{s}}{\mathrm{d}t}\,\mathrm{d}\mathbf{x}\right], \tag{85}$$

where $\langle\rangle_{\Gamma_2}$ denotes averaging over the top plate, S^* the dimensionless area of the cell, and x, y and t their dimensionless counterparts. Note that to derive (83) we assume $-q_y = k_\mathrm{f}\frac{\partial T_\mathrm{f}}{\partial y}$, so (83) is not valid if there are particles touching the top plate; at the contact region, the solid conductivity k_s rather than k_f should be used for the calculation of the heat flux.

It can be simply argued from (85) that the random motion of (solid or fluid) particles in the y-direction leads to a positive k_c. Suppose that one particle at y moves upwards Δy within Δt and gains a positive temperature increment ΔT. It has the same probability that this particle (or other particles) moves downwards Δy within Δt and undergoes a temperature drop ΔT. As a result, one gets a positive average $\langle y\frac{\mathrm{d}T}{\mathrm{d}t}\rangle \sim \Delta y\frac{\Delta T}{\Delta t} \sim \frac{(\Delta y)^2}{\Delta t}$. Since Δt needs to be small enough to capture each fluctuation of the particles in order to estimate the instantaneous temperature acceleration, $\frac{(\Delta y)^2}{\Delta t}$ here is not the long-term diffusion coefficient, but apparently, the fluctuating velocities of the particles (and the related diffusion coefficient) play an important role in the micro-convection-induced conductivity k_c. We will not compute k_c directly with (85) since it is more convenient to calculate k_e from (83) and k_d from (81).

Absence of convection effect: At very low Peclet numbers, the thermal convection effect can be neglected, therefore, there is no difference between the measured effective heat conductivity k_e and the molecular-heat-diffusion-related one k_d. The effective conductivity for the square array of circular particles was analyzed by Perrins et al. [59]. We compare our results obtained with meshes M1 and M3 to theirs in Fig. 13. Fig. 13a shows the comparison of the conductivity coefficient c defined in (81) in the dilute limit as a function of the conductivity ratio k_r. For our simulation, the dilute limit is approximated with placing one particle at the center of a $16d \times 16d$ square cell, which gives the particle area fraction of 0.00307. The further increase in the system size was found to lead to a slightly lower conductivity coefficient. Our results obtained with mesh M1 in Fig. 13a agree well with the analytical solution for $k_r < 5$, but the numerical error starts to become pronounced when k_r exceeds 5 and the relative error reaches up to 8% at $k_r = 40$. The finer mesh M3 is better used for high k_r since the accuracy of the solution can be significantly improved, as shown in Fig. 13a. Fig. 13b shows the comparison of the relative effective heat conductivity k_e/k_f for the square array as a function of the area fraction ϕ at $k_r = 5$. Four particles aligned with the y-axis are considered in our simulations because we found that the difference between the computed conductivities for four and eight particles are negligibly small. From Fig. 13b, the conductivities obtained with M1 are in good agreement with those of Perrins for $\phi < 0.4$ but higher than the latter for $\phi > 0.5$. A probable (primary) reason for this overestimation of the conductivity at high area fractions is that we use a homogeneous mesh for the fluid equations and the insufficient mesh resolution in the gap between particles results in the underestimation of the hindrance effect of the fluids on the heat conduction at $k_r > 1$. Not surprisingly, the accuracy of the solution at high ϕ is improved significantly by the use of M3 (recall that the fluid mesh resolution is also doubled accordingly), as shown in Fig. 13b. To sum up, our method with the coarse mesh M1 is reasonably accurate for the prediction of the conductivity of the composite particularly at relatively low k_r and ϕ. The choice of the fine mesh M3 is beneficial to the accuracy at high k_r or ϕ.

The conductivities of the random circular particle composite are calculated with a $16d \times 16d$ cell for $\phi \leqslant 0.52$ and are plotted in Fig. 13b. It is not surprising that they are slightly larger than those for the square array. The conductivities at high ϕ are not computed due to the difficulty in generating a random distribution of particles.

It should be noted that due to the numerical error the effective heat conductivity computed at the top plate (83) does not perfectly agree with the one computed at the particle boundary (81), but typically differs in the fourth digit, which is accurate enough in terms of the heat conductivity, but not for the calculation of the coefficient c in the dilute limit. We believe that c in the dilute limit is better calculated directly with (84).

Heat conductivity of sheared non-colloidal suspensions: Now we apply our method to analyze the heat conduction of non-colloidal suspensions in a Couette flow. The top and bottom plates move at different velocities,

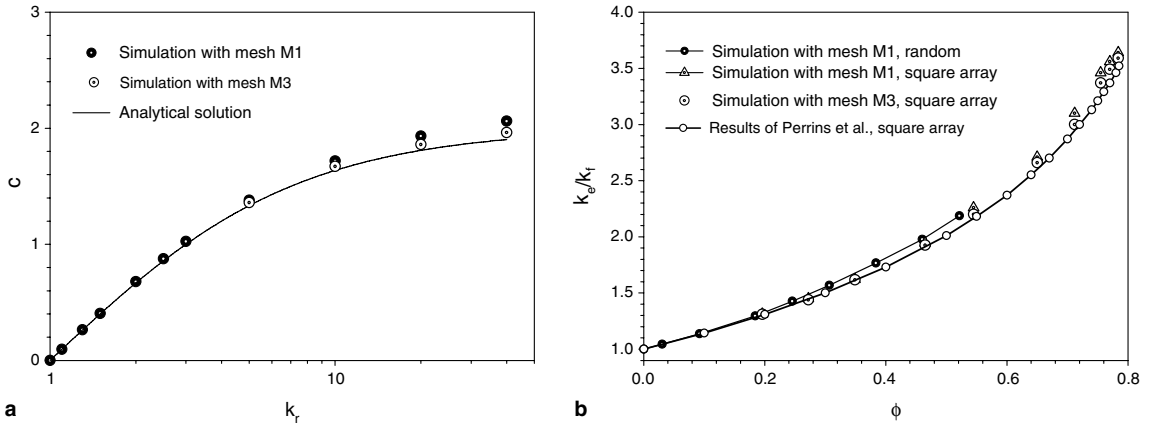

Fig. 13. (a) Effective heat conductivity coefficient c of a circular particle composite in the dilute limit as a function of the conductivity ratio k_r, as compared to the analytical solution $c = 2(k_r - 1)/(1 + k_r)$; (b) relative effective heat conductivities k_e/k_f at $k_r = 5$ as a function of the area fraction for the square array and random distribution of circular particles, respectively; the results of Perrins et al. [59] for the square array are plotted for comparison.

giving rise to a linear shear flow of the fluids. Suppose that the shear rate is $\dot{\gamma}$. We take the particle diameter d as the characteristic length and $d\dot{\gamma}$ as the characteristic velocity, so that the characteristic time is $(\dot{\gamma})^{-1}$. The effects of gravity and natural convection are not considered, i.e., $Fr = 0$ and $Gr = 0$. We here set $k_r = 5.0$, $c_{pr} = 1.0$ and $\rho_r = 1.001$.

We first examine the effect of the shear flow on the diffusion-related heat conductivity coefficient c defined in (81) in the dilute limit. A single particle is freely suspended at the center of $16d \times 16d$ Couette cell, the same geometry as the last problem. Fig. 14 shows the conductivity coefficient c at steady-state as a function of the Peclet number for $Re = 0.2$ and $Pr = 10$, respectively. It can be seen that the Peclet number has a negative effect on the conductivity coefficient c in case of keeping $Re = 0.2$, whereas the Reynolds number has a positive effect for the same Peclet numbers. Therefore, at a fixed Prandtl number, c is determined from the competition between the effects of Re and Pe: for $Pr = 10$, c decreases slightly at small Pe, then increases and reaches the maximum at $Pe \approx 30$, and then decreases again, as shown in Fig. 14. To explore the reason for such effects of Re and Pe, we plot in Fig. 15 the isotherms at four sets of (Re, Pe): $(0.2, 2)$, $(0.2, 50)$, $(3, 30)$ and $(5, 50)$. For $k_r > 1$, the conservation of the heat flux requires a smaller temperature gradient in the solid domain than in the fluids. Thus we can see in Fig. 15 that the isotherms are expanded when passing through the particle. From its definition (84), the value of c is determined from the average temperature gradient in the y-direction in the solid domain for a fixed k_r. Fig. 15a and b shows two effects of Pe on the isotherms: one is the declination of the isotherms, meaning the deviation of the maximum-temperature-gradient direction from the y-direction as a result of thermal convection; the other is the further increase in the gap between the isotherms, implying the deduction in the temperature gradient. Both effects give rise to a lower average temperature gradient in the y-direction (i.e., c) at a higher Peclet number. In contrast, a comparison between Fig. 15a and c indicates that the effect of Re can enhance the temperature gradient in the solid domain as a result of the enhanced fluid temperature gradient in the vicinity of the particle boundary at higher Re evidenced by the more crowded isotherms there, and a comparison between Fig. 15b and d reveals that the deviation of the maximum-temperature-gradient direction from the y-direction is also hindered by the effect of Re. The opposite effects of Re and Pe on c therefore are explained.

For the problems involving only a few particles, our homogeneous-mesh based DLM/FD method is not advantageous compared to the boundary-fitted methods in terms of accuracy and efficiency, although Fig. 15 shows that the moderately large discontinuity of the temperature gradient on the particle boundary for $k_r = 5$ appears to be nicely handled by our code. The power of the FD method lies in the simulation of moderately to highly concentrated suspensions of many particles. As an example, we simulate the motion of 800 particles in a $64d \times 32d$ Couette cell, which gives an intermediate area fraction $\phi = 0.307$. The computed relative diffusion-related conductivities and the average temperature gradients in the y-direction on the top plate at $Re = 0.2$ are depicted in Fig. 16. We were wrongly regarding the average temperature gradient on

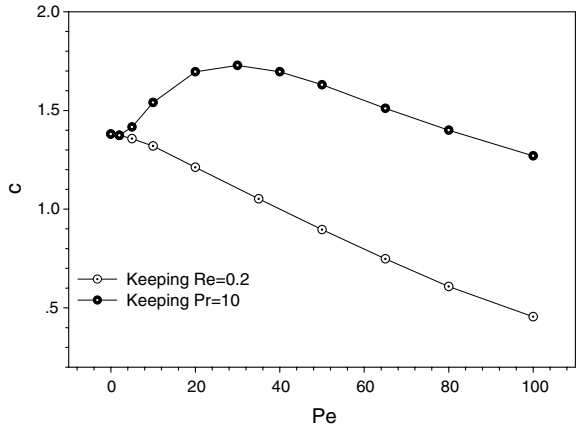

Fig. 14. Diffusion-related heat conductivity coefficient c of a sheared non-colloidal suspension of circular particles in the dilute limit as a function of the Peclet number for $Re = 0.2$ and $Pr = 10$, respectively. $\phi = 0.00307$, $k_r = 5.0$, $c_{pr} = 1.0$, $\rho_r = 1.001$, $Fr = 0$ and $Gr = 0$.

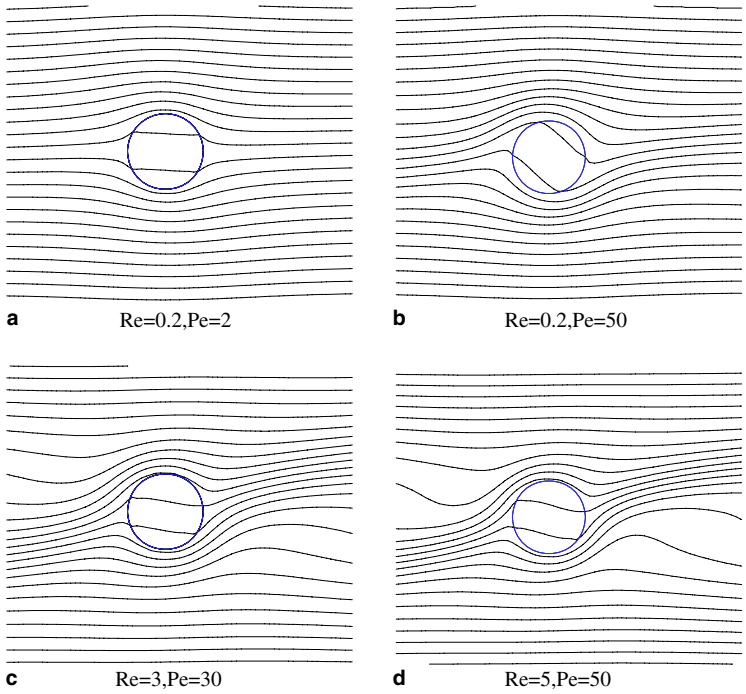

Fig. 15. Isotherms at steady-state for a circular particle freely suspended in a Couette flow at different Peclet and Reynolds numbers. The temperature increment for all contours is 0.163. $\phi = 0.00307$, $k_r = 5.0$, $c_{pr} = 1.0$, $\rho_r = 1.001$, $Fr = 0$ and $Gr = 0$.

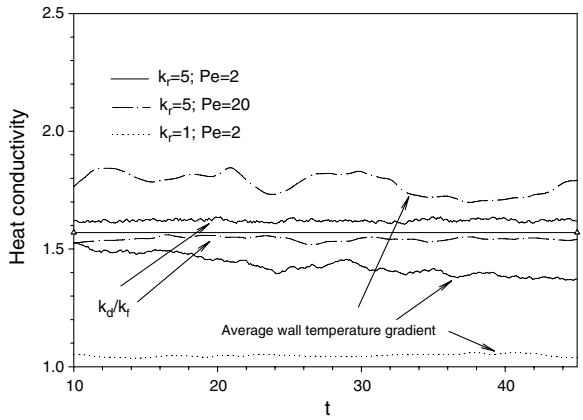

Fig. 16. Relative diffusion-related heat conductivity k_d/k_f and the dimensionless average temperature normal derivative on the top plate for a sheared non-colloidal suspension of circular particles. The line with symbols represents k_d/k_f for the random composite in the absence of flows. $\phi = 0.307$, $Re = 0.2$, $c_{pr} = 1.0$, $\rho_r = 1.01$, $Fr = 0$ and $Gr = 0$. $\Delta t = 0.0005$.

the top plate as the effective heat conductivity of the suspension from (83) and then surprised at the observation that the "effective" conductivity is smaller than the diffusion-related one for $k_r = 5$ and $Pe = 2$, which contradicts the simple argument mentioned earlier that the micro-convection-induced one is always positive for a diffusion system. We later realized that (83) is not valid in the present cases where they are many particles in near touch with the top plate (see Fig. 17) since in the derivation of (83) only the fluid conductivity is used to compute the heat flux on the plate. The overall decline in the average wall temperature gradient with time for $k_r = 5$ and $Pe = 2$ thus can be explained by the fact that there are more particles being occasionally pushed to the plate and then sticking there due to the lubrication force as time goes. For the case of $k_r = 1$, the average

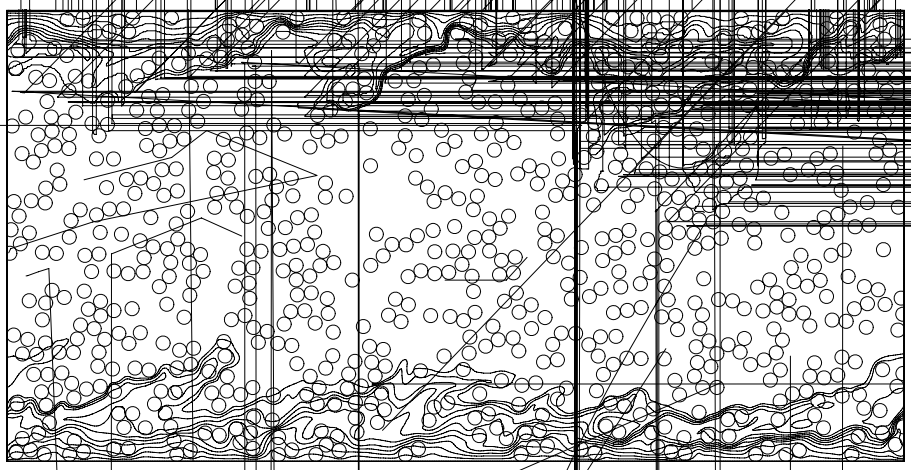

Fig. 17. Typical isotherms and particle configuration for a sheared non-colloidal suspension of 800 circular particles in a $64d \times 32d$ Couete cell. $\phi = 0.307$, $Re = 0.2$, $Pe = 20$, $k_r = 5$, $c_{pr} = 1.0$, $\rho_r = 1.001$, $Fr = 0$ and $Gr = 0$. $t = 30$.

temperature gradient equals k_c/k_f and becomes positive, as expected. For $k_r = 5$ and $Pe = 20$, it is also larger than k_d/k_f because the effect of thermal convection on k_c is so strong that it overshadows the negative effect due to the sticking particles. The typical isotherms for this case are displayed in Fig. 17, and one can see the substantially inhomogeneous temperature fields as a result of strong thermal convection at relatively large k_r.

For $k_r = 5$, $Re = 0.2$ and $Pe = 2$, we have observed that in the dilute limit the diffusion-related conductivity k_d decreases slightly compared to the one in the absence of flows, whereas the opposite is observed for $\phi = 0.307$ in Fig. 16, which is expected to be caused by the clusters of particles forming in the shear flow (Fig. 17) compared to the random distribution of particles when there are no flows. In addition, it is not surprising to find in Fig. 16 that the negative effect of Pe on k_d prevails at $Pe = 20$.

Heat conductivity of nanofluids: Nanofluids are essentially colloidal suspensions characterized by the strong Brownian motion of the suspended particles. The root-mean-square velocity of the Brownian particles u_B can be estimated from the energy equipartition law: $Mu_B^2 = n_d k_B T$, here n_d, k_B, T being the dimensionality of the motion, the Boltzmann constant and the absolute temperature of the suspension, respectively. Obviously, the Brownian velocity is increased dramatically as the particle size decreases, and Prasher et al. [33] has showed that the u_B-based particle Reynolds number is inversely proportional to the root of particle diameter $\sqrt{d}$ and can reach up to order O(0.01–0.1) for particles of a few nanometers suspended in water. Liquids normally have a large Prandtl number, thus the heat convection in the nanofluids could be pronounced and result in a significant contribution to the effective heat conductivity.

The Brownian effect can be numerically implemented by either introducing a random force into the equation of particle motion [60] or a random stress into the fluid momentum equations [61,62]. However, it is a non-trivial task to incorporate the Brownian effect in case of many particles into our direct simulation method with the either method in such a way that the fluctuation–dissipation theorem is exactly satisfied. Here, we use a very simple method that is by no means accurate but just for our attempt to confirm that the convection-related k_c can substantially contribute to the effective heat conductivity k_e at a relatively low Reynolds number of O(0.1) and a low particle volume fraction of O(0.01). In this method, the Brownian motion of each particle is considered separately by adding to the equation of particle motion (52) a random force $\mathbf{F}^B$ that is independent of the particle configuration and has a dimensional form as follows:

$$\mathbf{F}^B = \sqrt{\frac{2k_B T\xi}{\Delta t}}\Psi, \tag{86}$$

where ξ is the hydrodynamic friction coefficient and is obtained with a mean-field-like approximation to the resistance matrix, i.e., $\xi = \langle R \rangle$, and Ψ is the standard Gaussian deviate. In two dimensions, the forces in (52) (now including the Brownian force) are scaled as $\rho_f U_c^2 L_c$, and we let $\xi = K\eta$, K being a constant. With our definition of the characteristic velocity

$$MU_c^2 = k_B T, \tag{87}$$

one gets the dimensionless Brownian force

$$\overline{\mathbf{F}}^B = \sqrt{\frac{2\rho_r S_p^* K}{Re\Delta t}}\Psi. \tag{88}$$

In the derivation, we assume that the suspension has a homogeneous temperature T, as an approximation to the plate system where there is the temperature variance. The dimensionless temperature at the particle position would enter (88) if the temperature variance is accounted for. Note that Δt in (88) is the dimensionless time step scaled as L_c/U_c whereas Δt in (86) is dimensional. Again, we take the particle diameter as the characteristic length for the current Brownian simulations.

There are various methods to estimate the value of K, such as from $K\eta = \langle F\rangle/\langle U\rangle$ for a given force F or a given particle velocity U on each particle, and from the short-time diffusivity coefficient calculated with a method in [5]. We consider a 2D plate unit cell with both height and width being 32 particle diameters and there are 40 particles in the unit cell, corresponding to the area fraction of 0.0307. We found that the different methods give different K ranging from 6 to 15 for the random suspension at low Reynolds numbers. In our Brownian simulations, the gravitational effect and the natural convection are not considered, i.e., $Fr = 0$ and $Gr = 0$. With the density ratio ρ_r being fixed to be 1.01, the motion of the particles is governed by the Reynolds number and K. We set $K = 6$. From the energy equipartition law and the definition of the characteristic velocity (87), the computed dimensionless root-mean-square of the particle velocities u_B^* is expected to equal $\sqrt{2}$, however, its value calculated from our simulations is around 2.0 for both $Re = 0.1$ and $Re = 0.2$. The discrepancy is not surprising since the fluctuation–dissipation theorem is not exactly fulfilled in our simple method with $K = 6$. A more accurate algorithm for the Brownian motion based on the DLM/FD frame particularly for the 3D case is a subject of our future work; here we only conduct a qualitative study.

We let $k_r = 2.0$ and $c_{pr} = 1.0$. Fig. 18 shows the time evolutions of the calculated relative effective heat conductivities k_e/k_f and the relative diffusion-related conductivities k_d/k_f at $Re = 0.1$ and 0.2, and $Pe = 1$ and 2. We see that the effective conductivities are considerably larger than the diffusion-related ones, conforming that the convection-related conductivities k_c arising from the Brownian motion of the particles are large. The diffusion-related conductivities k_d are not sensitive to Re and Pe in the cases studied, and the values of k_d/k_f are around 1.021 (Fig. 18), being the same as the one in the absence of flows. In contrast, the convection-related conductivity k_c increases with increasing Re or Pe, as demonstrated in Fig. 18. Since both Re and Pe are low, the reason for the increase in k_c with Pe is mainly related to the coefficient Pe in the definition of k_c (85) and the one for Re is related to the integral in (85) that has been shown related to the Brownian diffusion of the particles earlier.

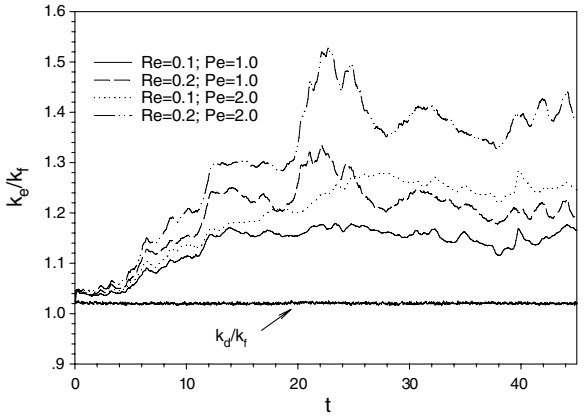

Fig. 18. Evolutions of the relative effective heat conductivities of nanofluids suspended with circular particles at different Reynolds and Peclet numbers in a 2D plate system with both height and width being 32 particle diameters. The results on the molecular-heat-diffusion-related conductivities k_d are also shown. The effects of gravity and natural convection are not considered. $\phi = 0.0307$, $k_r = 2.0$, $c_{pr} = 1.0$, $\rho_r = 1.01$ and $K = 6$. $\Delta t = 0.0005$.

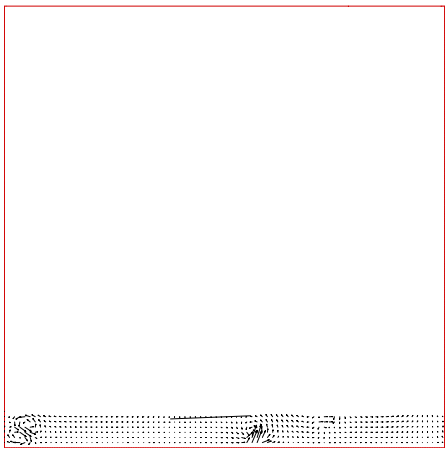

The typical structures of the flow and temperature fields are plotted in Fig. 19. The velocity of each particle fluctuates with time rapidly, and the velocities of the fluids in the vicinity of most particles appear to differ much in magnitude from the particle velocities (Fig. 19a), unlike the case of the steady motion of particles. However, the Brownian motion of the particles does carry a large amount of fluids to move with them in the general case (Fig. 19a) and consequently gives rise to a strong temperature convection (or fluctuation) of a length scale that is much larger than the particle size (Fig. 19b).

Our preliminary numerical results above support the argument that the micro-heat-convection in the fluids is responsible for the unusually high heat conductivity of nanofluids. However, a more accurate and 3D algorithm for the Brownian motion of nanoparticles is required to unambiguously elucidate the origin of the high heat conductivity. In addition, the validity of the continuum equations for nanofluids might need to be examined.

5. Conclusions

We have presented the DLM/FD methods for the heat transfer problems for both cases of fixed and freely varying temperatures on the immersed boundaries. The fluid-flow equations are solved with the finite-difference projection method on a half-staggered grid, as in our previous codes. In our operator splitting scheme, the Lagrange multipliers at the previous time level are kept in the fluid equations, and the new Lagrange multipliers for the rigid-body motion constraint and the Dirichlet temperature boundary condition are determined from the reduced saddle-point problem, whereas a very simple scheme based on the fully explicit computation of the Lagrange multiplier is proposed for the case of freely varying temperature on the particle boundary and is shown as accurate as the fully coupled scheme but limited to small $(\rho_r c_{pr} - 1)$. Our updated collision model based on the incorporation of the lubrication force is also briefly described.

Our code for the case of fixed temperature on the immersed boundary is verified by comparing favorably our results on the natural convection driven by a hot cylinder eccentrically placed in a square box and on the sedimentation of a cold circular particle in a vertical channel to the data in the literature. Our code for the case of freely varying temperature on the boundaries of freely moving particles is applied to analyze the motion of a catalyst particle in a box and in particular the heat conductivities of nanofluids and sheared non-colloidal suspensions, respectively. Our preliminary results support the argument that the micro-heat-convection in the fluids is responsible for the unusually high heat conductivity of nanofluids. It is observed that the Peclet number plays a negative role in the diffusion-related heat conductivity of a sheared non-colloidal suspension, whereas the Reynolds number does the opposite.

Although the method is implemented in two dimensions, the extension to the three-dimensional case is straightforward.

Acknowledgments

Y.Z. acknowledges the support from J.F. Brady and the Foundation for Fundamental Research on Matter (FOM) in the Netherlands. S.X. thanks the National Natural Science Foundation of China (No. 10472104) for the financial support.

References

[1] H.H. Hu, A. Patankar, M.Y. Zhu, Direct numerical simulations of fluid–solid systems using the arbitrary Lagrangian–Eulerian technique, J. Comput. Phys. 169 (2001) 427–462.
[2] A.J.C. Ladd, R. Verberg, Lattice-Boltzmann simulations of particle–fluid suspensions, J. Stat. Phys. 104 (2001) 1191–1251.
[3] K. Höfler, S. Schwarzer, Navier–Stokes simulation with constraint forces: finite-difference method for particle-laden flows and complex geometries, Phys. Rev. E 61 (2000) 7146–7160.
[4] R. Glowinski, T.-W. Pan, T.I. Hesla, D.D. Joseph, A distributed Lagrange multiplier/fictitious domain method for particulate flows, Int. J. Multiphase Flow 25 (1999) 755–794.
[5] A. Sierou, J.F. Brady, Accelerated Stokesian dynamics simulations, J. Fluid Mech. 448 (2001) 115–146.
[6] S. Lomholt, B. Stenum, M.R. Maxey, Experimental verification of the force coupling method for particulate flows, Int. J. Multiphase Flow 28 (2002) 225–246.
[7] S. Lomholt, M.R. Maxey, Force-coupling method for particulate two-phase flow: Stokes flow, J. Comput. Phys. 184 (2003) 381–405.
[8] R. Glowinski, T.-W. Pan, J. Périaux, A fictitious domain method for Dirichlet problems and applications, Comp. Meth. Appl. Mech. Eng. 111 (1994) 283–303.
[9] R. Glowinski, T.-W. Pan, J. Périaux, A fictitious domain method for external incompressible viscous flow modeled by Navier–Stokes equations, Comp. Meth. Appl. Mech. Eng. 112 (1994) 133–148.
[10] R. Glowinski, T.-W. Pan, J. Périaux, A Lagrange multiplier/fictitious domain method for the Dirichlet problem. Generalization to some flow problems, Jpn. J. Ind. Appl. Math. 12 (1995) 87–108.
[11] R. Glowinski, T.-W. Pan, J. Périaux, A Lagrange multiplier/fictitious domain method for the numerical simulation of incompressible viscous flow around moving rigid bodies (I): the case where the rigid body motions are known a priori, CR Acad. Sci. Paris 324 (1997) 361–369.
[12] F. Bertrand, P.A. Tanguy, F. Thibault, A three-dimensional fictitious domain method for incompressible fluid flow problems, Int. J. Numer. Meth. Fluids 25 (1997) 719–736.
[13] P.A. Tanguy, F. Bertrand, R. Labie, E. Brito-De La Fuente, Numerical modelling of the mixing of viscoplastic slurries in a twin-blade planetary mixer, Trans. IChemE 74 (Part A) (1996) 499–504.
[14] R. Glowinski, T.-W. Pan, T.I. Hesla, D.D. Joseph, J. Periaux, A fictitious domain approach to the direct numerical simulation of incompressible viscous flow past moving rigid bodies: application to particulate flow, J. Comput. Phys. 169 (2001) 363–426.
[15] Z. Yu, N. Phan-Thien, Y. Fan, R.I. Tanner, Viscoelastic mobility problem of a system of particles, J. Non-Newtonian Fluid Mech. 104 (2002) 87–124.
[16] Z. Yu, N. Phan-Thien, R.I. Tanner, Dynamical simulation of sphere motion in a vertical tube, J. Fluid Mech. 518 (2004) 61–93.
[17] W.R. Hwang, M.A. Hulsen, H.E.H. Meijer, Direct simulations of particle suspensions in a viscoelastic fluid in sliding bi-periodic frames, J. Non-Newtonian Fluid Mech. 121 (2004) 15–33.
[18] C.S. Peskin, Numerical analysis of blood flow in the heart, J. Comput. Phys. 25 (1977) 220–252.
[19] Z. Yu, A DLM/FD method for fluid/flexible-body interactions, J. Comput. Phys. 207 (2005) 1–27.
[20] X. Shi, N. Phan-Thien, Distributed Lagrange multiplier/fictitious domain method in the framework of lattice Boltzmann method for fluid–structure interactions, J. Comput. Phys. 206 (2005) 81–94.
[21] R. Mittal, G. Iaccarino, Immersed boundary methods, Annu. Rev. Fluid Mech. 37 (2005) 239–261.
[22] E.A. Fadlun, R. Verzicco, P. Orlandi, J. Mohd-Yusof, Combined immersed-boundary finite-difference methods for three-dimensional complex flow simulations, J. Comput. Phys. 161 (2000) 35–60.
[23] N.A. Patankar, P. Singh, D.D. Joseph, R. Glowinski, T.W. Pan, A new formulation of the distributed Lagrange multiplier/fictitious domain method for particulate flows, Int. J. Multiphase Flow 26 (2000) 1509–1524.
[24] S.C. Dong, D. Liu, M.R. Maxey, G.E. Karniadakis, Spectral distributed Lagrange multiplier method: algorithm and benchmark tests, J. Comput. Phys. 195 (2004) 695–717.
[25] M. Uhlmann, An immersed boundary method with direct forcing for the simulation of particulate flows, J. Comput. Phys. 209 (2005) 448–476.
[26] N. Sharma, N.A. Patankar, A fast computation technique for the direct numerical simulation of rigid particulate flows, J. Comput. Phys. 205 (2005) 439–457.
[27] Z. Feng, E.E. Michaelides, Proteus: a direct forcing method in the simulations of particulate flows, J. Comput. Phys. 202 (2005) 20–51.
[28] D. Kim, H. Choi, Immersed boundary method for flow around an arbitrarily moving body, J. Comput. Phys. 212 (2006) 662–680.

[29] F.P.T. Baaijens, A fictitious domain/mortar element method for fluid–structure interaction, Int. J. Numer. Meth. Fluids 35 (2001) 743–761.
[30] T.F. McKenna, R. Spitz, D. Cokljat, Heat transfer from catalysts with computational fluid dynamics, AIChE J. 45 (1999) 2392–2410.
[31] P. Keblinski, J.A. Eastman, D.G. Cahill, Nanofluids for thermal transport, Mater. Today 8 (2005) 36–44.
[32] J.C. Maxwell, A Treatise on Electricity and Magnetism, Clarendon, Oxford, 1873.
[33] R. Prasher, P. Bhattacharya, P.E. Phelan, Thermal Conductivity of Nanoscale Colloidal Solutions (Nanofluids), Phys. Rev. Lett. 94 (2005) 025901.
[34] S.P. Jang, S.U.S. Choi, Role of Brownian motion in the enhanced thermal conductivity of nanofluids, Appl. Phys. Lett. 84 (2004) 4316–4318.
[35] M. Nijemeisland, A.G. Dixon, CFD study of fluid flow and wall heat transfer in a fixed bed of spheres, AIChE J. 50 (2004) 906–921.
[36] H. Gan, J.Z. Chang, J.J. Feng, H.H. Howard, Direct numerical simulation of the sedimentation of solid particles with thermal convection, J. Fluid Mech. 481 (2003) 385–411.
[37] H. Gan, J.J. Feng, H.H. Howard, Simulation of the sedimentation of melting solid particles, Int. J. Multiphase Flow 29 (2003) 751–769.
[38] J. Kim, H. Choi, An immersed-boundary finite-volume method for simulations of heat transfer in complex geometries, K.S.M.E. Int. J. 18 (2004) 1026–1035.
[39] J.R. Pacheco, A. Pacheco-Vega, T. Rodić, R.E. Peck, Numerical simulations of heat transfer and fluid flow problems using an immersed-boundary finite-volume method on non-staggered grids, Numer. Heat Transf. Part B: Fundamentals 48 (2005) 1–24.
[40] V. Girault, P.-A. Raviart, Finite Element Methods for Navier–Stokes Equations: Theory and Algorithms, Springer-Verlag, Berlin, 1986.
[41] S. Armfield, R. Street, An analysis and comparison of the time accuracy of fractional-step methods for the Navier–Stokes equations on staggered grids, Int. J. Numer. Meth. Fluids 38 (2002) 255–282.
[42] W.H. Press, S.A. Teukolsky, W.T. Vetterling, B.P. Flannery, Numerical Recipes in FORTRAN: The Art of Scientific Computing, Cambridge University Press, Cambridge, 1992.
[43] C. Crowe, M. Sommerfeld, Y. Tsuji, Multiphase Flows with Droplets and Particles, CRC press, Boca Raton, FL, 1998.
[44] S.L. Dance, E. Climent, M.R. Maxey, Collision barrier effects on the bulk flow in a random suspension, Phys. Fluids 16 (2004) 828–831.
[45] N.Q. Nguyen, A.J.C. Ladd, Lubrication corrections for lattice-Boltzmann simulations of particle suspensions, Phys. Rev. E 66 (2002) 046708.
[46] D.J. Jeffrey, Y. Onishi, Calculation of the resistance and mobility functions for two unequal rigid spheres in low-Reynolds-number flow, J. Fluid Mech. 139 (1984) 261–290.
[47] B. Cichocki, R.B. Jones, Image representation of a spherical particle near a hard wall, Physica A 258 (1998) 273–302.
[48] J. Kromkamp, D.T.M. Van Den Ende, D. Kandhai, R.G.M. Van Der Sman, R.M. Boom, Shear-induced self-diffusion and microstructure in non-Brownian suspensions at non-zero Reynolds numbers, J. Fluid Mech. 529 (2005) 253–278.
[49] A. Sierou, J.F. Brady, Rheology and microstructure in concentrated noncolloidal suspensions, J. Rheol. 46 (2002) 1031–1056.
[50] I. Demirdžić, Ž. Lilek, M. Perić, Fluid flow and heat transfer test problems for non-orthogonal grids: bench-mark solutions, Int. J. Numer. Meth. Fluids 15 (1992) 329–354.
[51] R. Scardovelli, S. Zaleski, Direct numerical simulation of free-surface and interfacial flow, Annu. Rev. Fluid Mech. 31 (1999) 567–603.
[52] J.A. Sethian, P. Smereka, Level set methods for fluid interfaces, Annu. Rev. Fluid Mech. 35 (2003) 341–372.
[53] L. Zhu, C.S. Peskin, Simulation of a flapping flexible filament in a flowing soap film by the immersed boundary method, J. Comput. Phys. 179 (2002) 452–468.
[54] http:www.anter.com/6000.htm.
[55] G.K. Batchelor, The stress in a suspension of force-free particles, J. Fluid Mech. 41 (1970) 545–570.
[56] L.G. Leal, Macroscopic transport properties of a sheared suspension, J. Colloid Interf. Sci. 58 (1977) 296.
[57] J.F. Brady, G. Bossis, Stokesian dynamics, Annu. Rev. Fluid Mech. 20 (1988) 111–157.
[58] S. Lee, S.U.S. Choi, S. Li, J.A. Eastman, Measuring thermal conductivity of fluids containing Oxide Nanoparticles, Trans. ASME, J. Heat Transf. 121 (1999) 280–289.
[59] W.T. Perrins, R.C. McPhedran, D.R. McKenzie, Transport properties of regular arrays of cylinders, Proc. Roy. Soc., Ser. A 369 (1979) 207–225.
[60] A.J. Banchio, J.F. Brady, Accelerated Stokesian dynamics: Brownian motion, J. Comput. Phys. 118 (2003) 10323–10332.
[61] A.J.C. Ladd, Short time motion of colloidal particles: numerical simulation via a fluctuating lattice Boltzmann equation, Phys. Rev. Lett. 70 (1993) 1339–1342.
[62] N. Sharma, N.A. Patankar, Direct numerical simulation of the Brownian motion of particles by using fluctuating hydrodynamic equations, J. Comput. Phys. 201 (2004) 466–486.